Engineering Structures 284 (2023) 115969

Contents lists available at ScienceDirect

Engineering Structures

journal homepage: www.elsevier.com/locate/engstruct

Novel design procedure for steel hysteretic dampers in seismic retrofit of frame structures

Gloria Terenzi

Department of Civil and Environmental Engineering, University of Florence, Via S. Marta 3, 50139 Florence, Italy

ARTICLE INFO

Keywords:
Design procedures
Sizing criteria
Dissipative bracing systems
Steel dampers
Seismic assessment
Seismic retrofit

ABSTRACT

An energy-based design procedure for sizing dissipative bracing systems equipped with steel hysteretic dampers is proposed for application to the seismic retrofit of frame structures. The procedure is based on the following assumptions: it is not iterative, as it provides a direct estimation of the steel dissipater sizes; the stiffening effects of dampers reduce displacements below prefixed limits; their damping effects reduce displacements and stress states to keep the response of structural members within their safe domains up to medium-to-high levels of the input seismic action. The procedure is articulated in three steps: seismic assessment analysis in current state and definition of the elastic properties of the bracing system to be installed in the structure; design of the dampers; verification of the seismic performance of the structure in retrofitted conditions. A demonstrative case study concerning a precast reinforced concrete frame school building is offered to explicate the practical application of the procedure, as well as to evaluate the enhancement of its response generated by the intervention. The latter consists in incorporating a dissipative bracing system equipped with triangular-shaped added damping and stiffness (T-ADAS) steel hysteretic devices. The two limit hypotheses assumed in the computational analyses for the roof beam-to-column connections of the building, i.e. hinges or fixed-ends, allow to discuss how the fundamental period of the structure in current conditions affects the parameters involved in the sizing process of the T-ADAS dampers.

List of symbols:

a_g	Peak Ground Acceleration (PGA) for rigid soil;
F_0	spectral amplification factor;
C_u	coefficient of use of a structure;
T_{VN}, T_{VR}	nominal life and reference time period of a structure;
D_{des}	maximum displacement assumed as performance objective;
D_{min}	minimum displacement over which an acceptable energy dissipation can be produced by the dampers;
B_P, H_P, t_P	base, height, and thickness of T-ADAS damper plates;
$F_{P,y}$, $F_{P,u}$	yielding and ultimate forces of plates;
$d_{P,y}$, $d_{P,u}$	yielding and ultimate displacements of plates;
$k_{P,e}$, $k_{P,p}$	stiffness of the elastic and plastic response branches of plates;
$E_{D,1p,X(Y)}$	area of the equivalent hysteretic cycle of a damper constituting element (a plate in the case of T-ADAS devices), with maximum displacement $S_{des,1p,X(Y)}$ and force equal to $F_{p,y}$;
$E_{D,X(Y)}$	energy dissipation capacity of dampers;
$E^{HT}_{D,X(Y)}$, $E^{FT}_{D,X(Y)}$	energy dissipation capacity of dampers evaluated for the *HT* and *FT* schemes of case study structure;
$(E^{HT}_D)^{num}$, $(E^{FT}_D)^{num}$	numerical values of the total energy dissipated by the dampers, for the *HT* and *FT* schemes of case study structure;
E_I, E_D	input and dissipated energies;
f_{yk}, f_{tk}	yield stress and strength of steel;
$F^{CS}_{el,X(Y)}$, $F^{RS}_{el,X(Y)}$, $F^{HT-CS}_{el,X(Y)}$, $F^{HT-RS}_{el,X(Y)}$, $F^{FT-CS}_{el,X(Y)}$, $F^{FT-RS}_{el,X(Y)}$	base shear values for *CS, RS, HT-CS, HT-RS, FT-CS, FT-RS* conditions;
$F_{D,X(Y)}$, $F^{HT}_{D,X(Y)}$, $F^{FT}_{D,X(Y)}$	total damping force of the dissipaters in general, and for *HT, FT* conditions;
H_b	total building height;
$i_{X(Y)}$	total number of bays in *X*, or *Y* directions where are included the damped braces;
M	total building mass;
$M^{HT-CS}_{X(Y)}$, $M^{HT-RS}_{X(Y)}$, $M^{FT-CS}_{X(Y)}$, $M^{FT-RS}_{X(Y)}$	bending moments around *X* and *Y* axes at the column bases, for *HT-CS, HT-RS, FT-CS, FT-RS* conditions;
$K^{CS}_{el,X(Y)}$, $K^{RS}_{el,X(Y)}$, $K^{HT-CS}_{el,X(Y)}$, $K^{HT-RS}_{el,X(Y)}$ $K^{FT-RS}_{el,X(Y)}$,$K^{FT-RS}_{el,X(Y)}$	elastic stiffness of the structure, for *CS, RS, HT-CS, HT-RS, FT-CS, FT-RS* conditions;

E-mail address: gloria.terenzi@unifi.it.

https://doi.org/10.1016/j.engstruct.2023.115969
Received 24 October 2022; Received in revised form 3 March 2023; Accepted 6 March 2023
Available online 21 March 2023

$k_{i,A,X(Y)}^{RS}$, $k_{i,A,X(Y)}^{HT-RS}$, $k_{i,A,X(Y)}^{FT-RS}$ stiffness of a damper incorporated in the *i*-th bay of the structure, for *RS*, *HT-RS*, *FT-RS* conditions;
$k_{i,el,X(Y)}^{RS}$, $k_{i,el,X(Y)}^{HT-RS}$, $k_{i,el,X(Y)}^{FT-RS}$ elastic stiffness of the dissipative brace incorporated in the *i*-th bay of the structure, for *RS*, *HT-RS*, *FT-RS* conditions;
$k_{i,DA,X(Y)}^{RS}$, $k_{i,DA,X(Y)}^{HT-RS}$, $k_{i,DA,X(Y)}^{FT-RS}$ total stiffness of the dissipative brace incorporated in the *i*-th bay of the structure, for *RS*, *HT-RS*, *FT-RS* conditions;
$K_{DA,X(Y)}^{RS}$, $K_{DA,X(Y)}^{HT-RS}$, $K_{DA,X(Y)}^{FT-RS}$ total stiffness of the dissipative bracing system for *RS, HT-RS, FT-RS* conditions;
$K_{DAS,X(Y)}^{RS}$, $K_{DAS,X(Y)}^{HT-RS}$, $K_{DAS,X(Y)}^{FT-RS}$ stiffness of the retrofitted structure for *RS, HT-RS, FT-RS* conditions;
n_c number of hysteretic cycles with maximum $S_{des,1p,X(Y)}$ displacement of a T-ADAS damper plate;
$N_{p,X(Y)}$, $N_{p,X(Y)}^{HT}$, $N_{p,X(Y)}^{FT}$ total number of constituting elements of a damper (plates in the case of T-ADAS devices) in general, and for *HT*, *FT* conditions;
S subsoil category coefficient;
S_a, S_d pseudo-acceleration and displacement spectra;
S_{aN}, S_{dN} pseudo-acceleration and displacement spectra normalized to relevant maximum values;
$S_{a,max} = S_a(T_C)$ maximum value of the pseudo-acceleration spectrum (reached for $T = T_C$);
$S_{d,max} = S_d(T_D)$ maximum value of the displacement spectrum (reached for $T = T_D$);
S_a^{CS}, S_a^{RS} maximum pseudo-acceleration in *CS* and *RS* conditions;
$S_{des,X(Y)}$ design displacement of dampers;
$S_{des,1p,X(Y)}$ design displacement of each plate of dampers;
S_V ordinate of the constant pseudo-velocity spectrum branch;
T_C initial period of the constant pseudo-velocity spectrum branch;
T_D final period of the constant pseudo-velocity spectrum branch;
T^{CS}, T^{RS} fundamental periods of the structure in current and retrofitted conditions;
T_{INT} period corresponding to the intersection of the pseudo-acceleration and displacement spectra;
$T_{INT,A}$, $T_{INT,B}$, $T_{INT,C}$ values of T_{INT} for A-, B-, C-type soil;
$T_{el,X(Y)}^{CS}$, $T_{el,X(Y)}^{RS}$, $T_{el,X(Y)}^{HT-CS}$, $T_{el,X(Y)}^{HT-RS}$, $T_{el,X(Y)}^{FT-CS}$, $T_{el,X(Y)}^{FT-RS}$ fundamental periods corresponding to the elastic stiffness of the structure in *CS, RS, HT-CS, HT-RS, FT-CS, FT-RS* conditions;
$T_{DAS,X(Y)}^{RS}$, $T_{DAS,X(Y)}^{HT-RS}$, $T_{DAS,X(Y)}^{FT-RS}$ fundamental periods corresponding to the total stiffness of the structure in *CS, RS, HT-CS, HT-RS, FT-CS, FT-RS* conditions;
$u_{X(Y)}^{HT-CS}$, $u_{X(Y)}^{HT-RS}$, $u_{X(Y)}^{FT-CS}$, $u_{X(Y)}^{FT-RS}$ maximum response displacements for *HT-CS, HT-RS, FT-CS, FT-RS* conditions;
$V_{R,X(Y)}$ base shear strength;
$V_{X(Y)}^{HT-CS}$, $V_{X(Y)}^{HT-RS}$, $V_{X(Y)}^{FT-CS}$, $V_{X(Y)}^{FT-RS}$ maximum response base shears in *HT-CS, HT-RS, FT-CS, FT-RS* conditions;
η spectral damping factor$=\sqrt{\frac{10}{5+\xi}}$;
η^{CS}, η^{RS} spectral damping factors in *CS* or *RS* conditions;
$\left(\eta_{X(Y)}^{HT-RS}\right)^{num(V)}$, $\left(\eta_{X(Y)}^{FT-RS}\right)^{num(V)}$ η^{RS} values estimated from the numerical response in terms of base shears, for *HT-RS*, *FT-RS* conditions;
$\left(\eta_{X(Y)}^{HT-RS}\right)^{num(u)}$, $\left(\eta_{X(Y)}^{FT-RS}\right)^{num(u)}$ η^{RS} values estimated from the numerical response in terms of displacements, for *HT-RS*, *FT-RS* conditions;
ξ equivalent viscous damping ratio;
$\left(\xi_{X(Y)}^{HT-RS}\right)^{num(V)}$, $\left(\xi_{X(Y)}^{HT-RS}\right)^{num(V)}$ ξ^{RS} values estimated from the numerical response in terms of base shears for *HT-RS*, *FT-RS* conditions;
$\left(\xi_{X(Y)}^{HT-RS}\right)^{num(u)}$, $\left(\xi_{X(Y)}^{HT-RS}\right)^{num(u)}$ ξ^{RS} values estimated from the numerical response in terms of displacements for *HT-RS*, *FT-RS* conditions;
$\rho_{u,X(Y)}^{HT-CS}$, $\rho_{u,X(Y)}^{HT-RS}$, $\rho_{u,X(Y)}^{FT-CS}$, $\rho_{u,X(Y)}^{FT-RS}$ displacement ratios in *HT-CS, HT-RS, FT-CS, FT-RS* conditions;
$\rho_{V,X(Y)}^{HT-CS}$, $\rho_{V,X(Y)}^{HT-RS}$, $\rho_{V,X(Y)}^{FT-CS}$, $\rho_{V,X(Y)}^{FT-RS}$ base shear ratios in *HT-CS, HT-RS, FT-CS, FT-RS* conditions;
$\omega_{X(Y)}^{CS}$, $\omega_{X(Y)}^{RS}$, $\omega_{X(Y)}^{HT-CS}$, $\omega_{X(Y)}^{HT-RS}$, $\omega_{X(Y)}^{FT-CS}$, $\omega_{X(Y)}^{FT-RS}$ circular frequencies corresponding to $T_{el,X(Y)}^{CS}$, $T_{el,X(Y)}^{RS}$, $T_{el,X(Y)}^{HT-CS}$, $T_{el,X(Y)}^{HT-RS}$, $T_{el,X(Y)}^{FT-CS}$, $T_{el,X(Y)}^{FT-RS}$;
ΔS_{aN}^{η}, ΔS_{dN}^{η} normalized pseudo-acceleration and displacement spectra reductions for a given η factor value;
$\Delta S_{d,X(Y)}$, $\Delta S_{d,X(Y)}^{HT}$, $\Delta S_{d,X(Y)}^{FT}$ displacement spectra reductions in general, and for *HT, FT* conditions;
$\Delta T_{el,X(Y)}$, $\Delta T_{el,X(Y)}^{HT}$, $\Delta T_{el,X(Y)}^{FT}$ fundamental period reductions in general, and for *HT*, *FT* conditions;
$\Delta T_{TC-INT,ha}$ half value of the difference between T_{INT} and T_C periods for $\xi = 5$ %.

1. Introduction

Damping devices used for the seismic protection of new and existing structures can be classified according to several criteria, the oldest and most established of which is referred to the dependence of their hysteretic response on velocity or displacement [1–3]. This descends from Lazan's definition of hysteresis [4], whereby natural materials can exhibit a "rate dependent" or "rate independent" (also named "displacement dependent") cyclic behaviour, with or without recentering effects at the end of their response. From a technical viewpoint, this classification is not easy applied to quickly identify the most effective type of dampers in the seismic retrofit of building structures. Indeed, the capacity of supplying supplemental damping and horizontal translational stiffness generally depends both on the mechanical characteristics of dampers and their installation layout. By way of example, pressurized fluid viscous dampers, when mounted at the tip of supporting braces in parallel with the overlying beam axis [5], slightly increase the horizontal stiffness of the structural system, while supplying high additional damping. Instead, steel devices like ADAS (Added Damping and Stiffness [1–3,6,7]) dissipaters, typically provide significant contributions in terms of both properties, but conditionally to the plasticization of the constituting material. Therefore, the former type of dampers allows to reduce maximum forces and displacements almost only by means of the dissipated energy. On the contrary, when the devices have significant combined stiffening and damping capacities, the increase of stiffness produced by their installation reduces lateral displacements at the same time as forces increase. Thus, the intensity of the latter needs to be limited by the damping generated by the hysteretic response of this class of dissipaters. Moreover, in this case the protective system must be placed in symmetrical positions in plan, to prevent a growth of torsional response effects in the building [8,9]. This problem does not arise when almost only dissipative devices are used, since their incorporation does not significantly change the modal characteristics of the original structure [10–13].

The design of supplemental damping elements must be straightforwardly carried out both in terms of stiffness and damping, as the spreading of dissipative bracing technologies in the professional community strongly depends on the availability of simple design procedures, especially concerning the preliminary sizing stage.

Several methods have been proposed in the literature to this aim, the first ones of which fix a desired value of the damping ratio ξ (i.e. the ratio of the damping coefficient to the critical one) in the fundamental mode of vibration of the structure, when the associated effective modal mass (EMM) is a predominant portion of the total seismic mass [1,2,14–16]. The practical application of these methods consists in scaling the reference elastic response spectra by various damping ratios, and choosing the value that allows constraining the maximum "global" response parameters (base shear, top lateral displacements, etc) below targeted limits. When the devices are characterized by nonlinear viscous properties, these objectives can be met by transforming the characteristic damping coefficients of the dissipaters into equivalent linear viscous damping ones [3,15]. These studies laid down the basis of the design procedures of buildings incorporating passive energy dissipation systems included in ASCE 41-17 Standards [17].

A similar approach is adopted in procedures based on the use of normative response spectra scaled by reduction factors corresponding to the damping capacity of the devices [18,19]. Other methods use equivalent linear or non-linear static analyses to evaluate the design actions and reduce their effects by means of added damping [20–22]. All the above-mentioned procedures require iterative steps for their application and are conceived for substantially regular structures. A generalization to irregular structures in plan is presented in [23]. In [24] the design of hysteretic dampers is extended to take into account also the effects of the interaction of the frame structure with masonry infills, simulating both the in-plane and the out-of-plane seismic response of the latter.

An alternative approach is represented by an energy-based design criterion, originally proposed for pressurized fluid viscous dampers [5,25–26], and later extended to added damping and stiffness (ADAS) devices [27]. This criterion consists in determining the minimum damping coefficients of the devices required to assign them the capability of dissipating a prefixed fraction of the seismic input energy, E_I, computed either on each story [25,27] or the entire structure [26]. As this method requires a preliminary evaluation of the input seismic energy demand on the original structure, a finite element non-linear time-history analysis must be carried out at a first step. Then, E_I must be post-calculated from the results of this analysis.

With the aim of bypassing the need for a preliminary time-history analysis, a different energy-based design method has been proposed [10], to estimate the minimum damping capacity to be assigned to the dampers in order to reach pre-fixed reductions of the storey shears and/or inter-storey drifts computed in current conditions by means of a conventional elastic finite element analysis. This method has been formulated for almost only dissipative devices, such as the above-mentioned pressurized fluid viscous dampers.

By further developing this conceptual approach, a novel energy-based design procedure is proposed herein, where the energy dissipation demand is directly estimated for the whole structure, by simply referring to the pseudo-acceleration and displacement response spectra, rather than storey by storey, like in [10]. Thus, only a modal analysis is required to initialize the sizing process.

Furthermore, sizing is no more limited to almost only dissipative devices, but is extended to dampers characterized by joint stiffening and dissipative properties. Among this class, ADAS dampers [28–30] are expressly considered, and particularly T-ADAS type, i.e. constituted by T-shaped plates, as they offer greater ductility as compared to corresponding X-shaped ones [31]. The energy dissipation demand is directly estimated for the whole structure (instead of storey by storey, like in [10]), by means of the pseudo-acceleration and displacement response spectra (therefore, only the development of a modal analysis of the examined structures is required); this implicitly bypasses the need for preliminary time-history dynamic analyses, like in [10].

A detailed description of the design procedure is presented in the next Sections. A demonstrative application to the retrofit design of a precast reinforced concrete (RC) single-storey school building is then offered, to explicate relevant steps in practice. The structure is modelled by considering two limit conditions for the roof beam-to-column connections, i.e. hinges or fixed-ends, so as to generalize the study to any scheme in between the two extremes, which correspond to nearly cantilever or shear-type structures, respectively.

2. Objectives of the design procedure

The energy-based methodology proposed herein for sizing steel hysteretic dampers starts from the results of a preliminary linear elastic dynamic analysis of the bare frame (*BF*) building in current state (*CS*). The design objectives can be summarized as follows: 1) the procedure is not iterative; 2) stiffening effects produced by the dampers should reduce the displacements below a prefixed limit; 3) damping effects should primarily reduce the stress states of structural members (but also contribute to decrease displacements further), so as to keep their response inside, or slightly outside, relevant safe domains for seismic actions scaled up to the Basic Design Earthquake (BDE, with 10 % probability of being exceeded over the normative reference time period, V_R, for the considered type of structure and its use); in addition, the activation of plastic response should preferably start from the Serviceability Design Earthquake (SDE, with 63 % probability of being exceeded over V_R) to substantially limit non-structural damage too.

Objectives 1) and 3) are jointly pursued by estimating the energy dissipation demand on the dampers based on the area of their hysteretic cycles corresponding to targeted force and displacement reductions (ΔF and ΔS_d, respectively). This allows bypassing the evaluation of equivalent damping ratios ξ, or ductility-dependent parameters, as required by "classical" design methods, as commented in the Introduction.

Point 2) is pursued by imposing the fundamental periods of the retrofitted structure in the two main directions in plan to be included in the T vibration period interval ($[T_C, T_D]$) where the pseudo-velocity elastic response spectrum, S_V, is assumed to be a horizontal branch by most Seismic Standards. This assumption is motivated by the evidence of some damage scenarios, like the ones observed after the 2016–2017 Central Italy earthquake. Within these scenarios, non-negligible structural damage, and severe non-structural damage were surveyed for buildings with fundamental periods smaller than T_C retrofitted with dissipative braces incorporating steel dampers, an excessive stiffness of which delayed their plastic response, and thus the activation of the corresponding damping effects. Indeed, when the fundamental translational periods of the structure are small, namely close to T_C, the added stiffening effects caused by the dissipative braces tend to prevail over the damping ones, adversely increasing the maximum stress states in structural members. Based on this consideration, the proposed procedure suggests that the retrofit-related addition of lateral stiffness should not determine fundamental periods smaller than the T_C limit.

With the aim of explaining the use of spectral quantities to obtain prefixed performance objectives in retrofitted (*RS*) conditions, without passing from prefixed damping ratios, the correlation between pseudo-acceleration and displacement response spectra in the ($[T_C, T_D]$) interval is examined in the next Section, as a function of damping.

3. Correlation between pseudo-acceleration and displacement spectra

As highlighted by the graphs in Fig. 1, in the T period interval ($[T_C, T_D]$) characterized by a constant value of pseudo-velocity, S_V, the $S_a(T)$ pseudo-acceleration and $S_d(T)$ displacement spectra have an opposite trend with respect to their intersection point, located by the T_{INT} period. By way of example, Fig. 1 shows in superposition the BDE-scaled spectra referred to the Italian municipalities of L'Aquila (Fig. 1a-c) and Florence (Fig. 1d-f), evaluated for damping ratios ξ equal to 5 %, 10 %, 20 % and 28 %. The ordinates of these graphs are normalized to the maximum pseudo-acceleration $S_a(T_C)$ and displacement $S_d(T_D)$ values, respectively, to obtain the corresponding dimensionless spectra, $S_{aN}(T)$ and $S_{dN}(T)$. These are detailed for A- (rigid soil; Fig. 1a, 1d), B- (deposits of very thick sand, gravel or very stiff clay; Fig. 1b, 1e) and C-type (soft soil; Fig. 1c, 1f) soil categories, as defined by the Italian Standards [32], showing that the value of T_{INT} depends on the type of soil, but not on damping.

With the aim of defining the correlation between the $S_{aN}(T)$ and

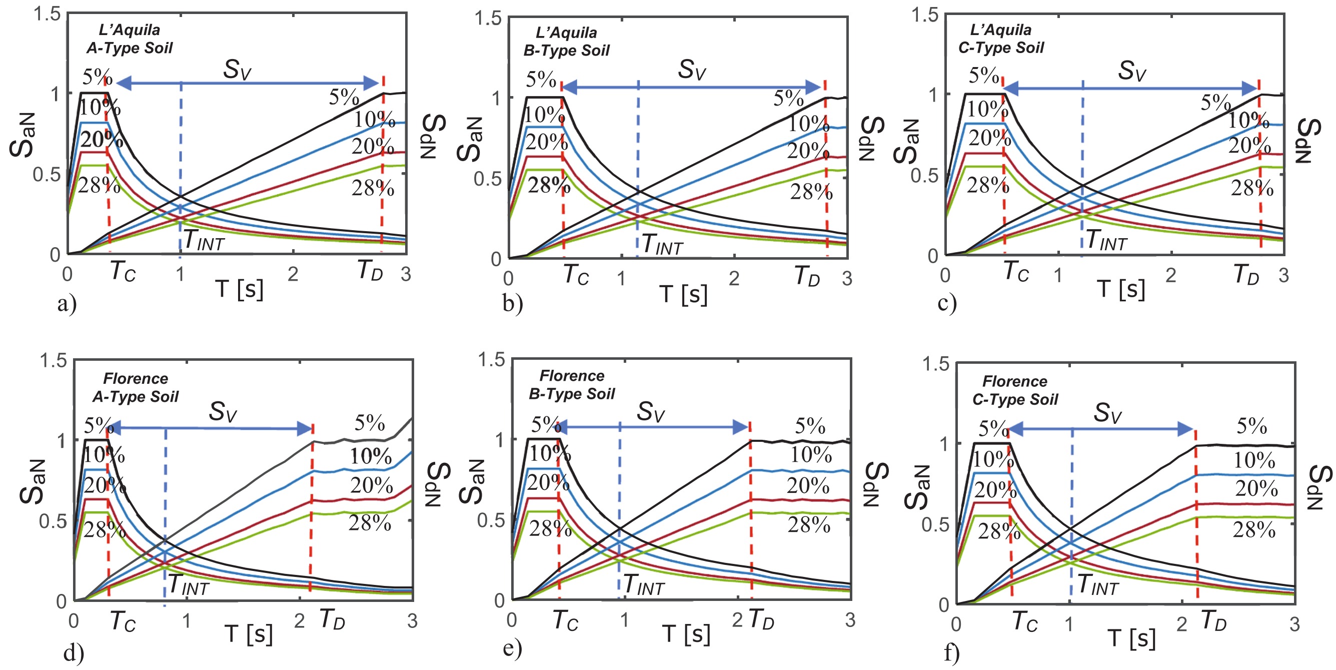

Fig. 1. Normalized pseudo-acceleration and displacement spectra for L'Aquila (1a-1c) and Florence (1d-1f).

$S_{dN}(T)$ spectral curves, their analytical functions are examined here by referring to the following parameters:

T^{CS}, T^{RS} = fundamental periods of the structure in current (T^{CS}) and retrofitted (T^{RS}) conditions, both included in the interval ([T_C, T_D]);

$$S_a = a_g S \eta F_0 \left(\frac{T_c}{T}\right) \tag{1}$$

$$S_d = S_a \left(\frac{T}{2\pi}\right)^2 \tag{2}$$

where:

a_g = peak ground acceleration (PGA) for rigid soil;

S = subsoil category coefficient;

η = spectral damping modification factor = $\sqrt{\frac{10}{5+\xi}}$;

F_0 = amplification factor;

ΔS^{η}_{aN}, ΔS^{η}_{dN} = variations of the pseudo-acceleration and displacement functions when passing from *CS* to *RS* conditions, for a generic η factor, normalized to the maximum pseudo-acceleration and displacement values, $S_{a,max} = S_a(T_C)$ and $S_{d,max} = S_d(T_D)$, respectively:

$$\Delta S^{\eta}_{aN} = \frac{S^{RS}_a - S^{CS}_a}{S_{a,max}} = \frac{a_g S F_0 T_C}{S_{a,max}} \left(\frac{\eta^{RS}}{T^{RS}} - \frac{\eta^{CS}}{T^{CS}}\right) \tag{3a}$$

$$\Delta S^{\eta}_{dN} = \frac{S^{RS}_d - S^{CS}_d}{S_{d,max}} = \frac{a_g S F_0 T_C}{4\pi^2 S_{d,max}} \left(\eta^{RS} T^{RS} - \eta^{CS} T^{CS}\right) \tag{3b}$$

By assuming to keep constant the equivalent linear viscous damping of the structure in *CS* and *RS* conditions, i.e. $\eta^{RS}=\eta^{CS} = \eta$, as normally accepted from a technical viewpoint, relations (3a), (3b) are simplified as follows:

$$\Delta S_{aN} = \frac{a_g S F_0 T_C}{S_a(T_C)} \left(\frac{\eta^{RS}}{T^{RS}} - \frac{\eta^{CS}}{T^{CS}}\right) = T_C \frac{(T^{CS} - T^{RS})}{T^{CS} T^{RS}} \tag{4a}$$

$$\Delta S_{dN} = \frac{a_g S F_0 T_C}{4\pi^2 S_d(T_D)} \left(\eta^{RS} T^{RS} - \eta^{CS} T^{CS}\right) = \frac{1}{T_D}\left(T^{RS} - T^{CS}\right) \tag{4b}$$

Named $\Delta T = T^{RS} - T^{CS}$ the period change occurring in the $CS \rightarrow RS$ transition, by deducing ($T^{RS} - T^{CS}$) from (4a) and (4b), the following equality is obtained:

$$-T_C T_D \Delta T = T^{CS} T^{RS} \Delta T \tag{5}$$

from which it follows:

$$-T_C T_D = T^{CS} T^{RS} \tag{6}$$

Thus, T_{INT} can be obtained from (6) by imposing $T^{CS} = T^{RS}$:

$$T_{INT} = \left|T^{CS}\right| = \left|T^{RS}\right| = \sqrt{T_C T_D} \tag{7}$$

By way of example, the T_{INT} values calculated by (7) for the spectral curves in Fig. 1, in the three soil type cases, are: $T_{INT,A}$ = 0,99 s, $T_{INT,B}$ = 1,16 s, $T_{INT,C}$ = 1,21 s (L'Aquila); $T_{INT,A}$ = 0,80 s, $T_{INT,B}$ = 0,95 s, $T_{INT,C}$ = 1,00 s (Florence), which match the T_{INT} values shown in Fig. 1.a-1.f.

If T^{RS} is smaller than T^{CS}, as a consequence of the stiffening effects of the retrofit intervention, and both are smaller than T_{INT}, an increase in pseudo-accelerations and a reduction in displacements is obtained in the $CS \rightarrow RS$ transition for a pre-fixed ξ value. The T^{RS} period can be initially estimated by applying (3b) for ξ = 5 % ($\eta^{CS} = \eta^{RS} = 1$), assuming a tentative $S_{d,max}$ value coinciding with a pre-established performance objective in terms of displacements, S_{des}. Relation (3a) can be used to preliminarily evaluate the amount of equivalent viscous damping needed to reduce S_a—and thus base shear and stress states—in addition to displacements. However, it is noted that the η^{RS} estimate derived from (3a) to achieve a target ΔS^{η}_{aN} value can be ineffective to evaluate the equivalent damping capacity of the dissipative braces, since it could significantly differ from the corresponding value determined by (3b). Moreover, η^{RS} could result remarkably below the lower limit of 0.55 (to which a value of ξ approximately equal to 28 % corresponds) of the η range of validity of the classical four-branch shapes of the pseudo-acceleration and displacement spectra assumed by most Seismic Standards [33–36]. As detailed in the next Sections, the proposed procedure bypasses this problem by defining the damping capacities of the dissipative braces, and thus of the incorporated devices, by directly evaluating the dissipated energy required to limit structural and non-structural damage in the retrofitted building, rather than separately targeting displacement and force reductions.

4. Formulation of the design procedure

The procedure estimates the damping capacity of steel devices, related to the plasticization of the constituting material, by referring to the area of the hysteretic cycles covered during seismic response [27]. For its practical implementation, the procedure is articulated in the following steps:

1. assessment of the structure in current conditions, and definition of the elastic properties of the bracing system;
2. sizing of the dampers;
3. multi-objective structural verification of the seismic response of the building in retrofitted conditions.

The three steps are detailed below and summarized in the flow-chart of Fig. 2.

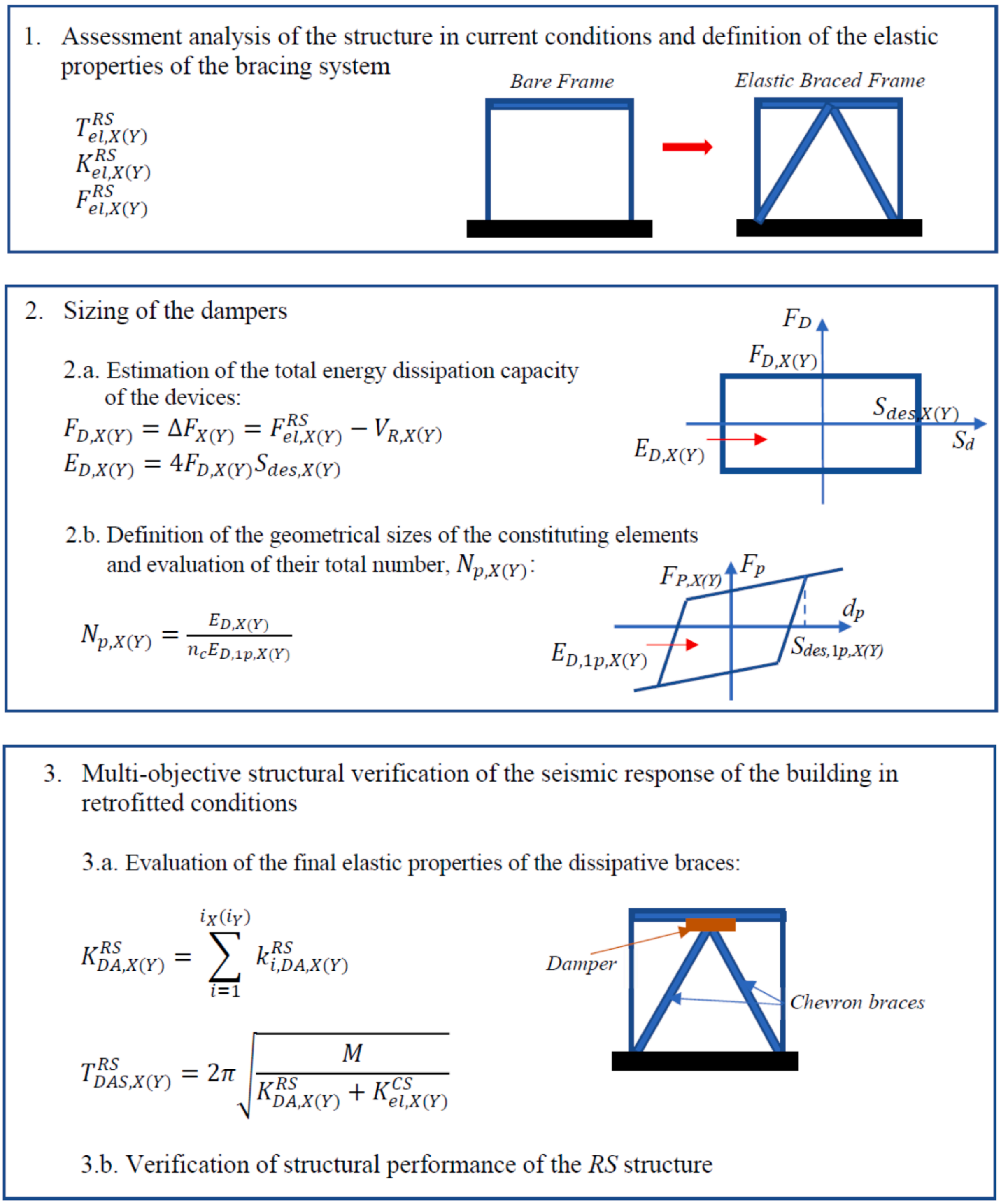

Fig. 2. Flow-chart of the design procedure.

4.1. First step: Assessment of the structure in current conditions and definition of the elastic properties of the bracing system

The first step consists in carrying out a modal analysis of the *BF* structure in *CS* conditions, to determine its fundamental translational periods, $T^{CS}_{el,X}$ and $T^{CS}_{el,Y}$, along the two reference axes in plan, *X* and *Y*.

Then, the values of the pseudo-acceleration, $S^{CS}_{a,X(Y)} = S_a\left(T^{CS}_{el,X(Y)}\right)$ are computed. The corresponding spectral displacement values, $S^{CS}_{d,X(Y)} = S_d\left(T^{CS}_{el,X(Y)}\right)$ are deduced by the expression:

$$S^{CS}_{d,X(Y)} = \left[\omega^{CS}_{X(Y)}\right]^2 S^{CS}_{a,X(Y)} \tag{8}$$

with $\omega^{CS}_{X(Y)}$ = circular frequency related to $T^{CS}_{el,X}$, or $T^{CS}_{el,Y}$.

Said *M* the total seismic mass of the structure, the elastic stiffness in *CS* conditions, $K^{CS}_{el,X(Y)}$, is given by:

$$K^{CS}_{el,X(Y)} = M\left[\omega^{CS}_{X(Y)}\right]^2 \tag{9}$$

from which the maximum base shear, $F^{CS}_{el,X(Y)}$, derives as follows:

$$F^{CS}_{el,X(Y)} = K^{CS}_{el,X(Y)} S^{CS}_{d,X(Y)} = M S^{CS}_{a,X(Y)} \tag{10}$$

Named D_{des} the maximum displacement assumed as performance objective, the elastic properties of the retrofitted structure can be estimated by determining the period and stiffness variations required to reduce the total displacement from $S^{CS}_{d,X(Y)}$ to D_{des}. Said $\Delta S_{d,X(Y)}$ this reduction:

$$\Delta S_{d,X(Y)} = S^{CS}_{d,X(Y)} - D_{des} \tag{11}$$

and S_V the pseudo-velocity constant value:

$$S_{V,X(Y)} = \omega^{CS}_{X(Y)} S^{CS}_{a,X(Y)} \tag{12}$$

the period variation $\Delta T_{el,X(Y)}$ is obtained as:

$$\Delta T_{el,X(Y)} = \frac{2\pi \Delta S_{d,X(Y)}}{S_{V,X(Y)}} \tag{13}$$

Consequently, in *RS* configuration the fundamental period, $T^{RS}_{el,X(Y)}$, the elastic stiffness, $K^{RS}_{el,X(Y)}$, and the maximum base shear, $F^{RS}_{el,X(Y)}$, are expressed as:

$$T^{RS}_{el,X(Y)} = T^{CS}_{el,X(Y)} - \Delta T_{el,X(Y)} \tag{14}$$

$$K^{RS}_{el,X(Y)} = M\left[\omega^{RS}_{X(Y)}\right]^2 \tag{15}$$

$$F^{RS}_{el,X(Y)} = M S^{RS}_{a,X(Y)} \tag{16}$$

where $\omega^{RS}_{X(Y)}$ and $S^{RS}_{a,X(Y)}$ are the circular frequency and pseudo-acceleration spectral values corresponding to $T^{RS}_{el,X(Y)}$. Since $F^{RS}_{el,X(Y)}$ could even significantly exceed the base shear strength, $V_{R,X(Y)}$ (given by the sum of the shear strength contributions of all vertical members, i.e. columns and shear walls), a reduction of forces is needed, and can be obtained thanks to the damping properties of the steel dampers.

4.2. Second step: Sizing of the dampers

This step implies the two following sub-steps: 2.a. estimation of the total energy dissipation capacity of the devices; 2.b. definition of the geometrical sizes and total number of constituting elements (represented by T-shaped plates, in the case of the T-ADAS dissipaters expressly considered in this study).

Step 2.a. According to the symbols and schemes in Fig. 2, the total damping force $F_{D,X(Y)}$ tentatively assigned to the sets of dampers to be installed in *X* and *Y* directions is given by the difference between the $F^{RS}_{el,X(Y)}$ and $V_{R,X(Y)}$ values calculated in the first step of the procedure:

$$F_{D,X(Y)} = F^{RS}_{el,X(Y)} - V_{R,X(Y)} \tag{17}$$

By referring to the idealized total plastic cycle (i.e. the hysteretic cycle net of the elastic portion) of the sets of dampers drawn in Fig. 2 (step 2.a) and Fig. 3, the target design plastic displacement of the dampers, $S_{des,X(Y)}$, can be fixed by distinguishing among the following three conditions: 1) $\Delta S_{d,X(Y)}$, given by (11), greater than the assumed limit displacement D_{des}; 2) $\Delta S_{d,X(Y)}$ smaller than D_{des} but greater than a minimum displacement value, D_{min}, representing the threshold over which an appreciable amount of energy dissipation is produced by the steel dampers; 3) $\Delta S_{d,X(Y)}$ smaller than D_{min}.

D_{des} can be deduced from the interstorey drift limitation imposed by the Italian Standards [32], as well as by several other Standards and Regulations, for the Immediate Occupancy performance level to prevent appreciable damage in drift-sensitive non-structural elements built in contact with the frame members, like traditional masonry infills and partitions, equal to 0.5 % of the interstorey height. Consistently with this assumption, and by approximately considering the same height for all storeys, D_{des} can be fixed at 0.5 % of the total height of the building, H_b (Fig. 3).

D_{min} threshold should be related to the yielding displacement of the selected type of steel dampers, so as to guarantee the activation of their plastic response starting from high-to-moderate seismic levels.

By referring to the spectral curves in Fig. 1, the first two conditions are met when $\Delta T_{el,X(Y)}$, expressed by (13), is greater than $\Delta T_{TC-INT,ha}$, defined as half the difference between T_{INT} and T_C periods, for ξ equal to 5 %:

$$\Delta T_{TC-INT,ha} = \frac{T_{INT} - T_C}{2} \tag{18}$$

Both in cases 1) and 2), $S_{des,X(Y)}$ can be assumed as the lowest of D_{des} and $\Delta S_{d,X(Y)}$. In case 3), where the stiffness of the original building is so high to cause a $\Delta S_{d,X(Y)}$ value smaller than D_{min}, S_{des} must be put as equal to D_{des}.

Based on the tentative values of the $F_{D,X(Y)}$ total damping force and the $S_{des,X(Y)}$ target plastic displacements of the devices, their total energy dissipation capacity, $E_{D,X(Y)}$, can be estimated by the following relation [5,10]:

$$E_{D,X(Y)} = 4F_{D,X(Y)} S_{des,X(Y)} \tag{19}$$

Step 2.b: Starting from the $E_{D,X(Y)}$ values estimated by (19), sizes and total number, $N_{p,X(Y)}$, of the constituting elements of a damper are defined by referring to the elasto-plastic response of a single element, sketched in Fig. 2 (step 2.b) and Fig. 3, where $S_{des,1p,X(Y)}$ and $E_{D,1p,X(Y)}$ are its target design displacement and energy dissipation capacity. For T-ADAS dampers, the geometry of a T-shaped steel plate is described in the left drawing of Fig. 4, where B_P, H_P and t_P represent its base, height and thickness. According to the nomenclature in the right drawing of Fig. 4, the parameters governing the idealized elasto-plastic force–displacement response cycle of a plate, $F_P(t)$-$d_P(t)$, namely: $F_{P,y}$ = yielding force, $d_{P,y}$ = yielding displacement, $k_{P,e}$ = stiffness of the elastic branch, $k_{P,p}$ = stiffness of the plastic branch, $F_{P,u}$ = ultimate force, $d_{P,u}$ = ultimate displacement, can be determined by the following relations [37–39]:

$$F_{P,y} = f_y \frac{B_P t_p^2}{6H_P} \tag{20}$$

$$d_{P,y} = \frac{F_{P,y}}{k_{P,e}} \tag{21}$$

$$k_{P,e} = \frac{E_s B_P t_p^3}{6H_P^3} \tag{22}$$

$$k_{P,p} = \gamma k_{P,e} \tag{23}$$

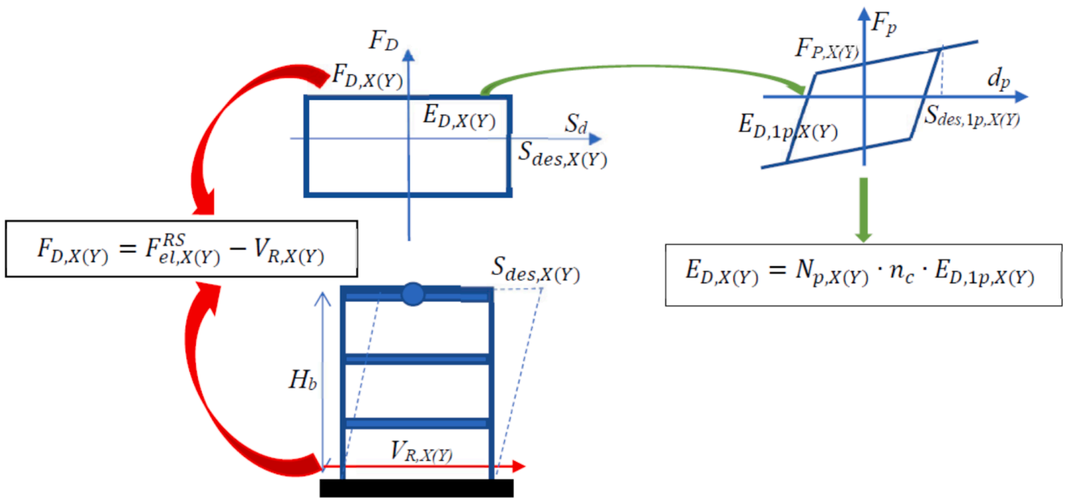

Fig. 3. Correlations among F_D, S_{des}, and the structural properties of the original structure.

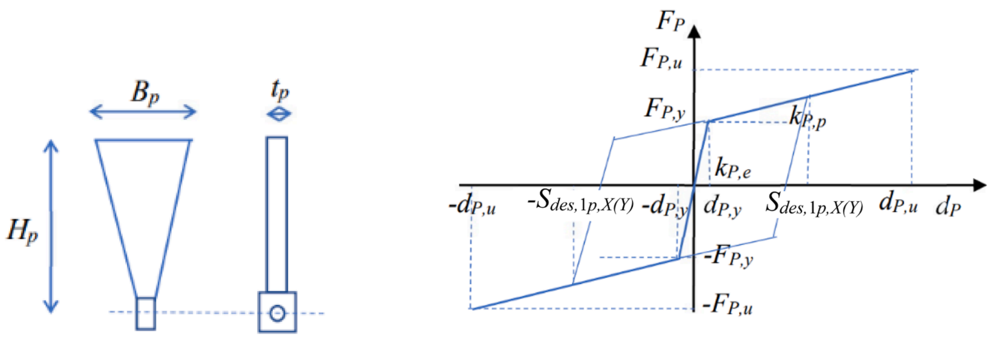

Fig. 4. Geometrical and mechanical parameters of the steel plates constituting the T-ADAS dampers.

$$F_{P,u} = f_y \frac{B_P t_p^2}{4H_P} \tag{24}$$

$$d_{P,u} = d_{P,y} + \frac{F_{P,u} - F_{P,y}}{k_{P,p}} \tag{25}$$

where: f_y, E_s = yielding stress and Young modulus of steel, and γ = strain hardening ratio characterizing the slope of the post-elastic branch, normally assumed as equal to 0.03 [37–39].

The $E_{D,1p,X(Y)}$ energy dissipation capacity of a plate can be evaluated by referring to the area of the hysteretic cycle with maximum displacement $S_{des,1p,X(Y)}$ and force equal to $F_{p,y}$. Similarly to expression (19), this area is given by:

$$E_{D,1p,X(Y)} = 4F_{P,y}S_{des,1p,X(Y)} \tag{26}$$

Based on the duration of the input seismic action and the values of the fundamental periods of the *RS* structure in *X* and *Y*, the total energy dissipated by a plate can be considered as equivalent to n_c times the area of the maximum response cycle covered for a considered seismic action, evaluated by (26). According to literature [27,40], n_c can be assumed to range from 4 to 14 for structures with fundamental periods lower than 1 s. As discussed in Section 5, n_c should be calibrated by considering the fundamental periods of the structure before and after retrofit, as well as the correlation between $\Delta T_{el,X(Y)}$ and $\Delta T_{TC-INT,ha}$. In particular, n_c ranges from 4 to 8 when $\Delta T_{el,X(Y)} > \Delta T_{TC-INT,ha}$, and from 9 to 14 for $\Delta T_{el,X(Y)} \leq \Delta T_{TC-INT,ha}$. This is motivated by the fact that the number of cycles developed by a plate is greater when it is incorporated in a stiffer structure (i.e. characterized by $\Delta T_{el,X(Y)} \leq \Delta T_{TC-INT,ha}$).

By referring to n_c, the $N_{p,X(Y)}$ total number of constituting elements (plates for T-ADAS devices) of the set of dampers to be adopted for the retrofit intervention is evaluated as follows:

$$N_{p,X(Y)} = \frac{E_{D,X(Y)}}{n_c E_{D,1p,X(Y)}} \tag{27}$$

For multi-storey buildings, the computed $N_{p,X(Y)}$ values must be distributed along the height proportionally to the interstorey drift demand assessed for the *BF* structure. Moreover, the installation of the devices in plan should minimize the distance between centre of mass and centre of stiffness at each storey, and thus the associated torsion response effects.

4.3. Third step: multi-objective structural verification of seismic response in retrofitted conditions

The third step comes with the two following sub-steps: 3.a. evaluation of the elastic properties of the bracing system and the total lateral stiffness of the retrofitted structure; 3.b. final verification of the seismic performance of the latter.

Step 3.a: The in-series arrangement of elastic-damping devices on top of the supporting inverse chevron braces causes to reduce the elastic stiffness of the *i*-th of the $i_{X(Y)}$ bays of the frame structure where the dampers are mounted, $k^{RS}_{i,el,X(Y)} = \frac{K^{RS}_{el,X(Y)}}{i_{X(Y)}}$, to the corresponding stiffness of the dissipative bracing system $k^{RS}_{i,DA,X(Y)}$, evaluated as:

$$k^{RS}_{i,DA,X(Y)} = \frac{k^{RS}_{i,el,X(Y)} k^{RS}_{i,A,X(Y)}}{k^{RS}_{i,el,X(Y)} + k^{RS}_{i,A,X(Y)}} \tag{28}$$

where $k^{RS}_{i,A,X(Y)}$ is the stiffness of the devices installed on the same bay. Thus, the total stiffness of the system, $K^{RS}_{DA,X(Y)}$ is given by the sum of the contributions of the i_X bays along X, and i_Y bays along Y, where it is incorporated:

$$K^{RS}_{DA,X(Y)} = \sum_{i=1}^{i_X(i_Y)} k^{RS}_{i,DA,X(Y)} \tag{29}$$

Then, the total lateral stiffness of the retrofitted structure is equal to the sum of $K^{RS}_{DA,X(Y)}$ and the $K^{CS}_{el,X(Y)}$ stiffness of the original structure. The corresponding periods in *RS* conditions are:

$$T^{RS}_{DAS,X(Y)} = 2\pi\sqrt{\frac{M}{K^{RS}_{DAS,X(Y)}}} = 2\pi\sqrt{\frac{M}{K^{RS}_{DA,X(Y)} + K^{CS}_{el,X(Y)}}} \tag{30}$$

Step 3.b: The final verification of the retrofitted structure, based on a time-history analysis carried out by means of a detailed finite element model, is aimed at checking whether the response to the earthquake levels considered in the design analysis meets the assumed performance objectives.

5. Geometrical and structural characteristics of the case study building

The case study examined for a demonstrative application of the design criterion is a nursery school built in Florence in the early 1970s. The building is a single-storey RC precast structure, composed of two asymmetrically joined blocks, named 1 and 2 in the structural plan of Fig. 5, where the reference coordinate axes, the fixed alignments and the numbering of columns are shown too. The longitudinal cross section parallel to the 3*X* fixed alignment is represented in Fig. 6. The dimensions of the two blocks in plan are equal to 16.00 × 15.65 m × m (Block 1) and 15.70 × 15.85 m × m (Block 2). The above-ground height of the building, H_b, is equal to 3.30 m.

The structure is constituted by three types of precast "Omega"-shaped RC beams, named B_A, B_B, and B_C in Fig. 7a-c, and identical precast RC columns, with dimensions of 300 × 300 mm × mm (Fig. 7d). As highlighted in the plan, the beams of Block 2, parallel to *Y*, have 2.70 m long end-cantilever spans. The roof floor is composed of T-shaped prefabricated RC purlins, parallel to *X*, placed at a mutual distance of 1040 mm, with 510 mm-high T-shaped section, including a 60 mm-thick upper RC slab (Fig. 7e).

The ground floor is made of the same T-shaped purlins, which are orthogonally oriented with respect to the roof ones. Foundations are smoothed socket-type, with a hollow core where the bottom end zone of columns is grouted. The infills of the building are made of traditional double-layer (the hollow bricks outside, solid bricks inside) masonry panels.

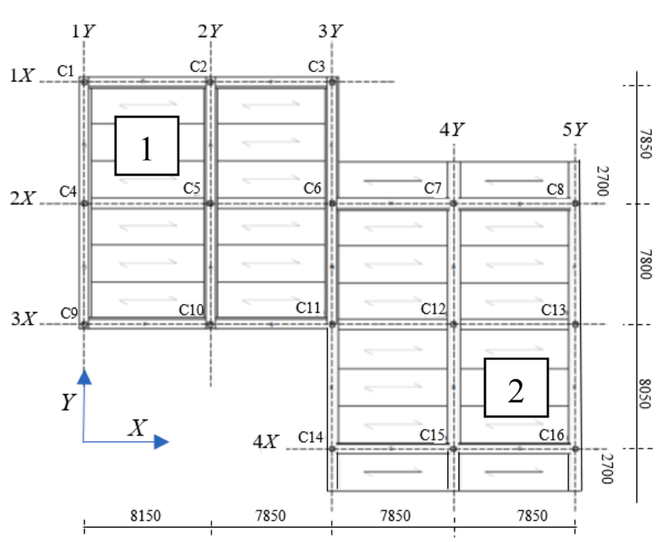

Fig. 5. Structural plan of the case study building (dimensions in millimeters).

An investigation campaign was carried out on materials and structural members, including on-site Son-Reb, pacometric and Vickers-type micro-durometer analyses, and laboratory tests on concrete and steel bar samples. Tests on beam-to-column connections were not carried out due to the inherent difficulties in developing them. Consequently, the seismic assessment analysis of the building was developed by hypothesizing hinge (*HT*) and fixed-end (*FT*) limit conditions for the beam-to-column joints, and thus a cantilever-like (*HT*) and near shear-type (*FT*) behaviour of the structure under lateral loads. The following mechanical properties were estimated from the results of the testing campaign: mean cubic compressive strength of concrete equal to 23.6 N/mm^2; yield stress and limit stress of steel equal to 430.5 MPa and 594 MPa, respectively. The total seismic mass of the building computed from the load analysis is equal to 390.7 kN/g.

6. Assessment analysis in current conditions

The assessment study of the structure, constituting Step 1 of the procedure, was articulated in a preliminary modal analysis, and a non-linear time-history analysis. The structure was modelled by means of SAP2000NL software [41], introducing hinged (*HT*), or fixed end (*FT*) constraints on top of columns, as observed above. The results obtained for the two limit cases, both in current (*CS*) and retrofitted (*RS*) conditions, are discussed in the next Sections. A view of the finite element model of the structure, generated by using frame-type elements for all members, is displayed in Fig. 8.

The analysis was carried out for the three upper reference seismic levels fixed in the Italian Standards [30], i.e. Serviceability Design Earthquake (SDE, with 63 % probability of being exceeded over the reference nominal structural life T_{VR}), Basic Design Earthquake (BDE, with 10 %/T_{VR} probability), and Maximum Considered Earthquake (MCE, with 5 %/T_{VR} probability). The T_{VR} period is fixed at 75 years, which is obtained by multiplying the nominal structural life T_{VN} of 50 years by a coefficient of use C_u equal to 1.5, imposed to buildings whose seismic resistance is of importance in view of the consequences associated with their possible collapse, like the case-study school. By referring to topographic category T1 (flat surface), and B-type soil (deposits of very thick sand, gravel or very stiff clay) for the site where the building is located, the resulting peak ground accelerations for the three seismic levels are the following: 0.078 *g* (SDE), 0.181 *g* (BDE), and 0.227 *g* (MCE) for the horizontal components; 0.022 g (SDE), 0.079 g (BDE), and 0.111 g (MCE) for the vertical ones. Relevant pseudo-acceleration elastic response spectra at linear viscous damping ratio $\xi = 5$ % are shown in Fig. 9.

Time-history analyses were developed by assuming artificial ground motions as inputs, generated in families of seven by SIMQKE-II software [42] from the pseudo-acceleration spectra above. As required by the Italian Standards [32], as well as by several other international seismic Codes and Regulations [17,43], in each time-history analysis the accelerograms were assumed in groups of two simultaneous horizontal components, with the former selected from the first generated family of seven motions and the latter selected from the second family, plus the vertical component.

6.1. Analysis in the HT-CS hypothesis

The modal analysis carried out by referring to the *HT* scheme in current state (*HT-CS*) shows two first translational modes along *X* and *Y*, with periods of 0.92 s (*X*), $T^{HT-CS}_{el,X}$, and 0.90 s (*Y*), $T^{HT-CS}_{el,Y}$, respectively, and effective modal masses (EMMs) of about 98.8 % for both directions. The third mode is purely rotational around the vertical axis *Z*, with period of 0.735 s, and EMM equal to 99.9 %.

The results of the analyses carried out at the SDE are evaluated in terms of maximum horizontal roof displacements, $u^{HT-CS}_{X(Y)}$, and their ra-

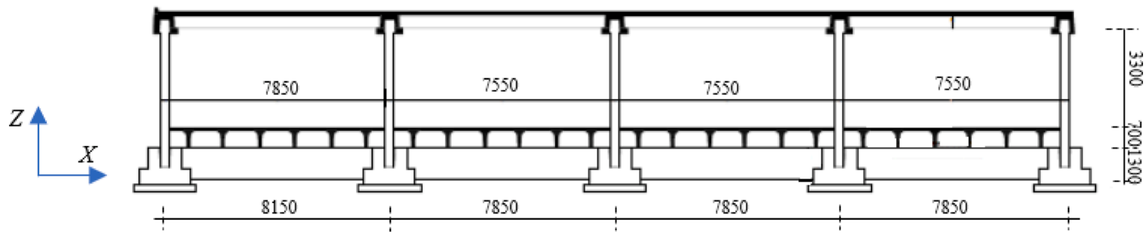

Fig. 6. Cross section of the building along the 3*X* fixed alignment (dimensions in millimeters).

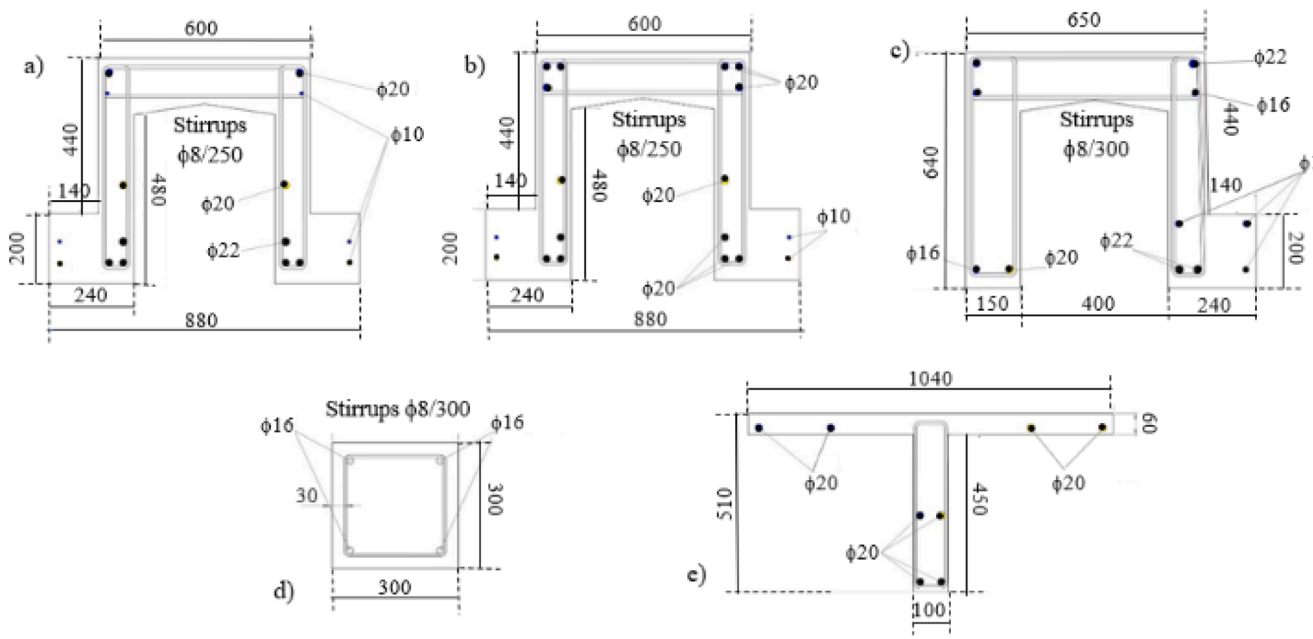

Fig. 7. Redrawn cross sections of: a) B_A-type beams; b) B_B-type beams; c) B_C-type beams; d) columns; and e) purlins (dimensions in millimeters).

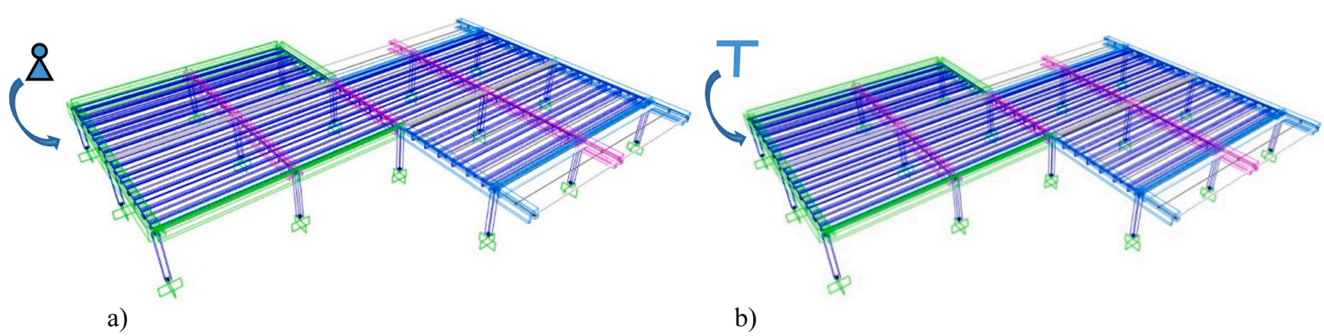

Fig. 8. View of the finite element model of the *HT*- (a) and *FT*- (b) structure, differing for the roof beam-to-column connections.

tios to the building height, $\rho_{u,X(Y)}^{HT-CS}$ (Table 1). The peak $\rho_{u,X(Y)}^{HT-CS}$ values induced by the most severe among the seven groups of input motions are as follows: 0.59 % in *X*, and 0.49 % in *Y*. The former is greater, and the latter a bit smaller, than the above-mentioned Immediate Occupancy-related interstorey drift limit of 0.5 %, herein assumed as D_{des}.

The computed $\rho_{u,X(Y)}^{HT-CS}$ values are equal to 1.29 % (*X*) and 1.13 % (*Y*) at the BDE, 1.68 % (*X*) and 1.36 % (*Y*) at the MCE, assessing moderate-to-high (BDE) and high (MCE) potential plastic demands on columns, should an inelastic—instead of elastic—finite element analysis be carried out, and very severe (BDE) to extremely severe (MCE) damage of infills. According to Italian Standards, the performance level attained in terms of displacement response is Life Safety (LS), both for the BDE and the MCE.

The response to the two upper seismic levels was assessed also in terms of base shear and stress states. Table 2 reports the maximum base shear values, $V_{X(Y)}^{HT-CS}$, and their ratios, $\rho_{V,X(Y)}^{HT-CS}$, to relevant strength values, $V_{R,X(Y)}$, where the latter are equal to: $V_{R,X} = V_{R,Y} = 550.3$ kN. By focusing on the analyses carried out at the BDE, the $V_{X(Y)}^{HT-CS}$ and $\rho_{V,X(Y)}^{HT-CS}$ values result as follows: 788.9 kN (V_X^{HT-CS}) and 740.4 kN (V_Y^{HT-CS}); 1.43 ($\rho_{V,X}^{HT-CS}$) and 1.34 ($\rho_{V,Y}^{HT-CS}$), assessing unsafety factors greater than 40 % (*X*) and 30 % (*Y*). Concerning the response of columns, neither the shear-related stress state checks nor the combined axial force-biaxial bending moment checks are met in both directions.

By way of example of the latter checks, Fig. 10 shows the combined response histories of the bending moments around the two axes, M_X^{HT-CS},

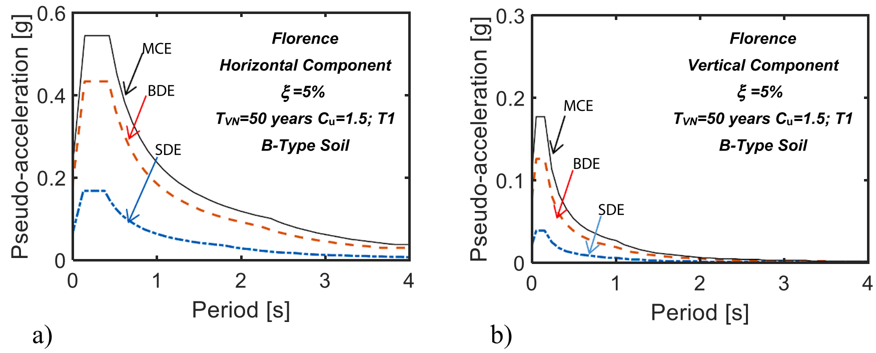

Fig. 9. Normative pseudo-acceleration elastic response spectra for Florence: horizontal (a) and vertical (b) components.

M_Y^{HT-CS}, obtained from the most demanding among the seven groups of BDE- and MCE-scaled accelerograms, for columns C1, C11 and C16 (according with the nomenclature in Fig. 5). The boundary of the safe interaction domain of these columns, traced out for the value of the axial force referred to the basic combination of gravity load, is also drawn in these graphs. The response curves highlight maximum M_X^{HT-CS}–M_Y^{HT-CS} values significantly exceeding the safe domain boundary. Indeed, they result 1.75 (bending moment around *X*) and 1.49 (bending moment around *Y*)—C1 column, 1.84 (*X*) and 1.66 (*Y*)—C11, and 1.88 (*X*) and 1.84 (*Y*)—C16 times greater than the corresponding values situated on the boundary, at the BDE, and 2.32 (*X*) and 1.88 (*Y*)—C1, 2.46 (*X*) and 2.14 (*Y*)—C11, and 2.53 (*X*) and 2.36 (*Y*)—C16 times, at the MCE. The mutual differences between the moment ratio values for the columns situated in opposite positions in plan, i.e. C1 and C16 (equal to 7.1 % in *X*, and 18.4 % in *Y*, for the BDE; and 8.3 % in *X*, and 20.3 % in *Y*, for the MCE), show relatively low torsion effects on the structure.

6.2. Analysis in the FT-CS hypothesis

The modal analysis carried out on the *FT* model in *CS* conditions (*FT-CS*) shows two first horizontal translational modes along *X* and *Y*, with vibration periods $T_{el,X}^{FT-CS}$, $T_{el,Y}^{FT-CS}$, equal to 0.498 s, and 0.472 s, respectively, and EMMs equal to 98.6 % in *X* and 93.3 % in *Y*. As for the *HT* scheme, the third mode is purely rotational around the vertical axis *Z*, with period of 0.426 s and EMM equal to 92.8 %.

The results of the time-history analyses developed at the SDE are evaluated in terms of maximum displacements, $u_{X(Y)}^{FT-CS}$, and their ratios to the building height, $\rho_{u,X(Y)}^{FT-CS}$, in this case too. As reported in Table 3, the $\rho_{u,X(Y)}^{FT-CS}$ values induced by the most severe among the seven groups of input motions are as follows: 0.33 % in *X*, and 0.35 % in *Y*, i.e. coinciding with, or close to, the 0.33 % interstorey drift limit fixed by Italian Standards for the Operational performance level. The $\rho_{u,X(Y)}^{FT-CS}$ values computed for the BDE and MCE are: 0.83 % (*X*) and 0.73 % (*Y*)—BDE, 1.06 % (*X*) and 0.94 % (*Y*)—MCE, to which moderate damage on columns, and moderate-to-severe damage on infills (BDE), and moderate-to-severe damage on columns and severe damage on infills (MCE) can be associated. All these displacement-related damage levels are lower than the ones evaluated for the *HT* scheme. This result is consistent with the notably higher lateral stiffness of the *FT* scheme.

Similarly to Table 2 for the *HT*-related analyses, Table 4 summarizes the results obtained in terms of maximum base shears, $V_{X(Y)}^{FT-CS}$, and their ratios, $\rho_{V,X(Y)}^{FT-CS}$, to relevant strength values, $V_{R,X(Y)}$, for the SDE, BDE and MCE. As expected for this stiffer scheme, $\rho_{V,X(Y)}^{FT-CS}$ values are significantly greater than the *HT*-related ones. By focusing attention on the response at the BDE, $V_{X(Y)}^{FT-CS}$ values result as follows: 1373 kN (V_X^{FT-CS}) and 1509 kN (V_Y^{FT-CS}), giving rise to base shear ratios of 2.49 ($\rho_{V,X}^{FT-CS}$) and 2.74 ($\rho_{V,Y}^{FT-CS}$). Like for the *HT* model, neither the shear stress state checks nor the combined axial force-biaxial bending moment checks on columns are met.

The biaxial moment response curves shown in Fig. 10 for the *HT* case are duplicated in Fig. 11 for the *FT* scheme, highlighting that maximum M_X^{FT-CS}–M_Y^{FT-CS} combined values significantly exceed the safe domain boundary in this configuration too, with peaks up to 20 % greater for the fixed-end hypothesis. Indeed, the moments in Fig. 11 are 1.88 (around *X*) and 1.71 (around *Y*)—C1 column, 1.94 (*X*) and 1.78 (*Y*)—C11, and 2.12 (*X*) and 1.94 (*Y*)—C16 times greater than the corresponding values situated on the safe domain boundary, for the BDE, and 2.45 (*X*) and 2.03 (*Y*)—C1, 2.42 (*X*) and 2.26 (*Y*)—C11, and 2.69 (*X*) and 2.48 (*Y*)—C16 times at the MCE. As observed for the *HT-CS* scheme, the differences between the values of the moment ratios for columns C1 and C16 (11.3 % in *X*, and 11.7 % in *Y*, for the BDE; 9.1 % in *X*, and 18.3 % in *Y*, for the MCE) identify little torsion effects in plan for the *FT-CS* case too.

7. T-ADAS Dissipative bracing retrofit solutions

By referring to the nomenclature in Fig. 4, the geometric sizes initially selected for the plates of the T-ADAS devices are as follows: H_p = 150 mm, t_p = 15 mm, and B_p = 75 mm. The constituting steel is S275 type, with yield stress and tensile strength equal to f_{yk} = 275 N/mm^2 and f_{tk} = 430 N/mm^2, respectively. The application of the sizing procedure of the dampers is presented below separately for the *HT* and *FT* configurations.

7.1. Retrofit intervention in the HT hypothesis

Step 1.

As observed in Section 6.1, the main translational periods of the *HT-CS* structure ($T_{el,X}^{HT-CS}$ = 0.92 s, $T_{el,Y}^{HT-CS}$ = 0.90 s), are both slightly smaller than the T_{INT} value, equal to 0.95 s (Fig. 1f). The corresponding $S_{a,X}^{HT-CS}$ and $S_{a,Y}^{HT-CS}$ pseudo-acceleration values at the BDE can be estimated from the graphs in Fig. 9. They result to be equal to 0.20 g ($S_{a,X}^{HT-CS}$) and 0.204 g ($S_{a,Y}^{HT-CS}$). Then, the $S_{d,X(Y)}^{HT-CS}$ spectral displacement values can be estimated from (2), obtaining: 42.1 mm ($S_{d,X}^{HT-CS}$) and 41.1 mm. Therefore, by assuming D_{des} = 0.5 % H_b = 0.005·3300 = 16.5 mm, the following design parameters are obtained by applying (11) through (14): $\Delta S_{d,X}^{HT}$ = 25.6 mm; $\Delta S_{d,Y}^{HT}$ = 24.5 mm; S_V = 287.5 mm/s; $\Delta T_{el,X}^{HT}$ = 0.559 s; $\Delta T_{el,Y}^{HT}$ = 0.538 s; $T_{el,X}^{HT-RS}$ = 0.36 s; $T_{el,Y}^{HT-RS}$ = 0.364 s.

The $T_{el,X(Y)}^{HT-RS}$ periods, both smaller than T_C, equal to 0.427 s, are used to size the inverted chevron brace sections, starting from the corresponding $K_{el,X(Y)}^{HT-RS}$ stiffness values. This assumption is not in contrast with the objective of determining fundamental periods greater than T_C for the retrofitted building. Indeed, as shown in the next step of the procedure, the in-series connection between chevron braces and dampers produces a lateral stiffness $K_{DAS,X(Y)}^{HT-RS}$ of the *HT-RS* structure smaller than $K(T_C)$ =

Table 1
CS and *RS* conditions for *HT* scheme: maximum displacements $u^{HT}_{X(Y)}$ and $\rho^{HT}_{u,X(Y)}$ ratios.

CS/RS	D_{des} (mm)	SDE				BDE				MCE			
		u_X^{HT-RS}(mm)	u_Y^{HT-RS}(mm)	$\rho_{u,X}^{HT-RS}$(%)	$\rho_{u,Y}^{HT-RS}$(%)	u_X^{HT-RS}(mm)	u_Y^{HT-RS}(mm)	$\rho_{u,X}^{HT-RS}$(%)	$\rho_{u,Y}^{HT-RS}$(%)	u_X^{HT-RS}(mm)	u_Y^{HT-RS}(mm)	$\rho_{u,X}^{HT-RS}$(%)	$\rho_{u,Y}^{HT-RS}$(%)
HT-CS	16.5	19.7	16.4	0.59	0.49	43.3	39.5	1.29	1.13	55.7	44.9	1.68	1.36
HT-RS	16.5	6.8	7.3	0.2	0.22	18.0	14.6	0.54	0.44	23	18.5	0.69	0.56

84603 kN/m, considered as an upper threshold for the retrofitted building. By referring to $K^{HT-RS}_{el,X(Y)}$, tubular profiles with external diameter of 42.4 mm and thickness of 2.5 mm are selected for the diagonal trusses. Moreover, due to the fact that $T^{HT-RS}_{el,X}$ and $T^{HT-RS}_{el,Y}$ are included in the period range with constant pseudo-acceleration, equal to $S_a(T_C)$, the $F^{HT-RS}_{el,X(Y)}$ base shears are assumed as equal to the $F_{el}(T_C)$ value computed by means of relation (16), by multiplying the $M = 390.7$ kN/g total mass of the building by $S_a(T_C) = 0.427$ g, i.e. $F^{HT-RS}_{el,X} = F^{HT-RS}_{el,Y} = F_{el}(T_C) = 390.7{\cdot}0.427{\cdot}g = 1648.2$ kN.

Step 2.

2.a. The $E^{HT}_{D,X(Y)}$ energy dissipation capacity of the dampers is evaluated by referring to the equivalent damping force $F^{HT}_{D,X(Y)}$ calculated by relation (17): $F^{HT}_{D,X} = F^{HT}_{D,Y} = 1097.9$ kN. In this case: $\Delta S^{HT}_{d,X} = 25.6$ mm, $\Delta S^{HT}_{d,Y} = 24.9$ mm, which are both greater than D_{des}. Based on the observations in Section 4.2, the S_{des} design displacement of the dissipaters, which is the minimum between ΔS_d and D_{des}, is put as equal to D_{des} for both directions. Thus, $E^{HT}_{D,X(Y)}$ is obtained by means of (19): $E^{HT}_{D,X} = E^{HT}_{D,Y}=$ 72.5 kJ.

2.b. The following values of the energy dissipation demand per plate are derived from (26), for $S_{des} = D_{des}$: $E^{HT}_{D,1p,X} = E^{HT}_{D,1p,Y} = 0.325$ kJ. Moreover, as $\Delta T_{el,X(Y)}$ is greater than $\Delta T_{TC-INT,ha}$, n_c is tentatively assumed as equal to 5, within the ([4,8]) interval discussed above, in order not to oversize the dissipaters. Consequently, the total number of plates given by relation (27) results to be: $N^{HT}_{p,X}$=$N^{HT}_{p,Y} \sim 45$. By rounding this value, 48 plates in X and 48 plates in Y are adopted. The plates are assembled in groups of 12, symmetrically placed on the 4 bays highlighted in blue along X, and red along Y, in the plan of Fig. 12. It is observed that the four internal bays selected for the installation (D2X, D3X, D2Y, D3Y) constitute the perimeter of the building hall, which is bounded by the partitions situated on the four plan alignments defined by columns C5 through C7, and C10 through C12. This positioning does not interfere with the free functioning of this portion of the building. At the same time, it does not obstruct access to the classrooms, since the inverse chevron layout of braces allows introducing a door in between each pair of diagonal trusses when the partitions are rebuilt, leaving the architectural arrangement of the interiors unchanged.

Step 3.

3.a. The final evaluation of the elastic properties of the dissipative braces is carried out by considering the in-series connection of diagonal trusses and plates. By applying (28), where $k^{HT-RS}_{i,A,X} = k^{HT-RS}_{i,A,Y} = 12{\cdot}k_{P,e} = 12{\cdot}2625.7 = 31508$ kN/m is the elastic stiffness of each T-ADAS device composed of 12 plates, and $k^{HT-RS}_{i,el,X} = k^{HT-RS}_{i,el,Y} = 25201$ kN/m is the elastic stiffness of each inverted chevron brace along the two axes, the stiffness values of the in-series system, $k^{HT-RS}_{i,DA,X}$ and $k^{HT-RS}_{i,DA,Y}$, result to be both equal to 14,000 kN/m.

Consequently, the increased stiffness produced by the 4 + 4 damped braces incorporated in the structure is equal to $K^{HT-RS}_{DA,X} = K^{HT-RS}_{DA,Y}=$ 56,001 kN/m. By considering that $K^{HT-CS}_{el,X}$, $K^{HT-CS}_{el,Y}$ are 18,222 kN/m and 19,044 kN/m, respectively, the following fundamental periods of the retrofitted structure are estimated by (30): $T^{HT-RS}_{DAS,X} = 0.456$ s; $T^{HT-RS}_{DAS,Y} = 0.453$ s.

3.b. The verification step of the *HT-RS* structure performance starts from the results of the modal analysis in retrofitted conditions, which shows two first translational modes along X and Y, with nearly coincident vibration periods, equal to 0.474 s (X), and 0.462 s (Y), and EMMs of 69.6 % (X), and 69.8 % (Y), respectively. The third mode is rotational around Z, with period of 0.403 s, and EMM equal to 94.3 %. The first two periods are close to the corresponding values calculated by relation (30), $T^{HT-RS}_{DAS,X(Y)}$, which differ by about 4 % in X, and 2 % in Y.

The bottom line of Table 1 offers a list of maximum drifts, $u^{HT-RS}_{X(Y)}$, and drift ratios, $\rho^{HT-RS}_{u,X(Y)}$, for the *HT-RS* structure, obtained from the

Table 2
CS and *RS* conditions for the *HT* scheme: maximum base shears $V^{HT}_{X(Y)}$ and $\rho^{HT}_{s,X(Y)}$ ratios.

CS/RS	$V_{R,X(Y)}$ (kN)	SDE				BDE				MCE			
		V_X^{HT-RS}(kN)	V_Y^{HT-RS}(kN)	$\rho_{s,X}^{HT-RS}$	$\rho_{s,Y}^{HT-RS}$	V_X^{HT-RS}(kN)	V_Y^{HT-RS}(kN)	$\rho_{s,X}^{HT-RS}$	$\rho_{s,Y}^{HT-RS}$	V_X^{HT-RS}(kN)	V_Y^{HT-RS}(kN)	$\rho_{s,X}^{HT-RS}$	$\rho_{s,Y}^{HT-RS}$
HT-CS	550.3	363	337	0.66	0.61	789	740	1.43	1.34	1055	956	1.92	1.74
HT-RS	550.3	371	389	0.67	0.70	629	559	1.14	1.01	761	655	1.38	1.19

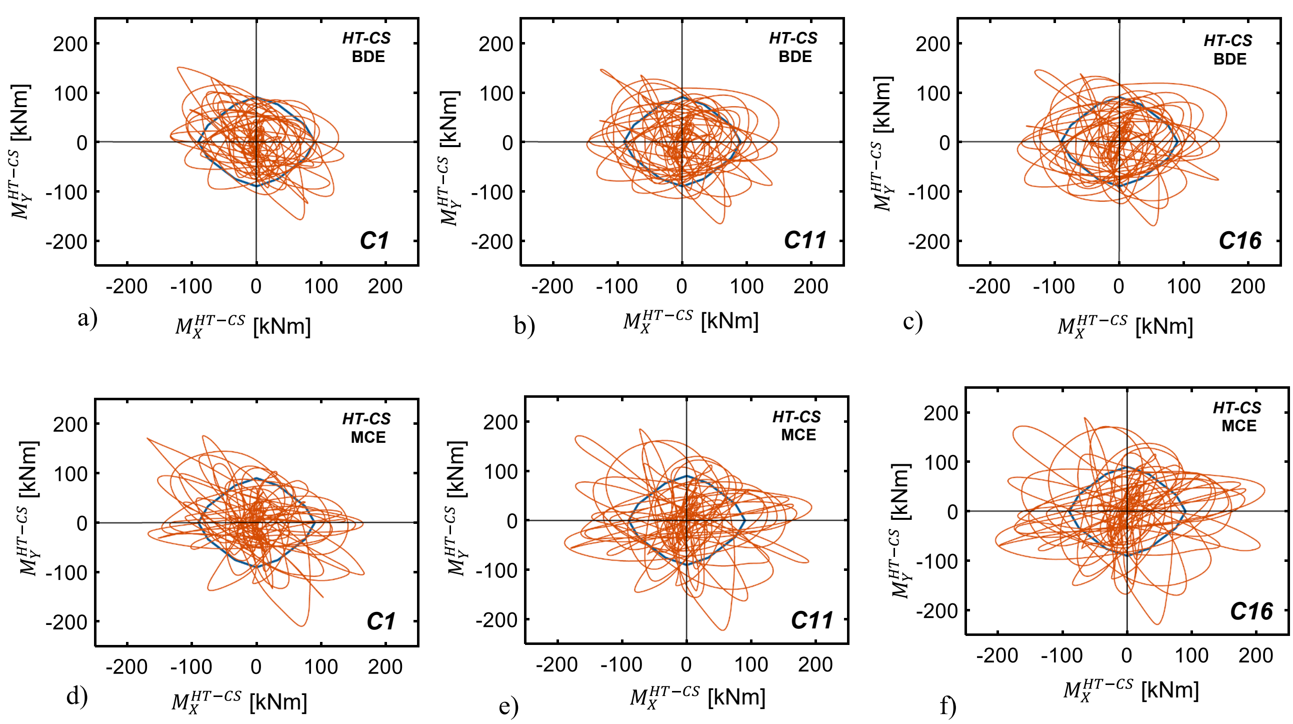

Fig. 10. *HT-CS* structure. M_X^{HT-CS}–M_Y^{HT-CS} biaxial moment interaction curves at the base section of C1, C11, and C16 columns obtained from the most demanding BDE-scaled (a, b, c) and MCE-scaled (d, e, f) groups of accelerograms, and relevant biaxial moment safe domains.

numerical analyses carried out by the SDE-, BDE- and MCE-scaled accelerograms. At the SDE, the $\rho^{HT-RS}_{u,X(Y)}$ values are as follows: 0.20 % in *X*, and 0.22 % in *Y*, both lower than the Operational performance level limitation of 0.33 %. The $\rho^{HT-RS}_{u,X(Y)}$ values computed for the two upper earthquake levels are: 0.54 % (*X*) and 0.44 % (*Y*) at the BDE, 0.69 % (*X*) and 0.56 % (*Y*) at the MCE, to which no damage to columns, and negligible (BDE) and low (MCE) damage to infills and partitions, is related.

By comparing these data with the corresponding values in current conditions, reduction factors on the drift ratios equal to 58 % (*X*) and 61 % (*Y*) at the BDE, and 59 % both in *X* and *Y* at the MCE are found, assessing a considerable performance enhancement in terms of lateral displacements produced by the retrofit intervention.

The results in terms of maximum base shears $V^{HT-RS}_{X(Y)}$, and their ratios to relevant strength values, $\rho^{HT-RS}_{V,X(Y)}$, are summarized in the bottom line of Table 2. Maximum percent differences equal to about 14 % (*X*) with the tentative values estimated by the procedure are observed at the BDE. More specifically, the incorporation of the protective system allows to decrease the base shear ratios from 1.43 % to 1.14 % (*X*) and from 1.34 % to 1.01 % (*Y*) at the BDE, and from 1.92 % to 1.38 % (*X*) and from 1.74 % to 1.19 % (*Y*) at the MCE. The slightly lower reductions obtained in *X* direction are a consequence of the lower energy dissipated by the set of T-ADAS devices placed in this direction (D_{1X}-D_{4X}) equal to 63 kJ, as compared to the dampers in *Y* (D_{1Y}-D_{4Y}), equal to 80 kJ. These values are 13 % lower (*X*), and 10 % greater (*Y*) than the $E^{HT}_{D,X(Y)}$ amounts estimated at step 2 of the design procedure. At the same time, by computing the total dissipated energy in the two directions, the difference between the value estimated by expression (19), $E_D^{HT} = 145$ kJ, and the value computed from the results of the finite element analysis, $(E_D^{HT})^{num} = 143$ kJ, is no greater than 1.3 %.

The response in terms of biaxial bending moments at the C1, C11 and C16 column bases, displayed by the graphs in Fig. 13, is constrained within relevant safe domains at the BDE. The boundaries of the domains are exceeded at most by 12 % for column C16, along *Y*, at the MCE.

The activation of dampers starting from the SDE is proved by the hysteretic cycles plotted in Fig. 14, referred to the D_{1X} and D_{4Y} devices (similar responses are obtained for the remaining ones).

The total number of equivalent cycles n_c is derived from the results of the time-history analysis, by computing the total energy dissipated by a single plate, equal to 1.31 kJ in *X* and 1.66 kJ in *Y*, and dividing these values by the energy dissipated in the cycle characterized by the maximum plastic displacement (13.8 mm in *X*, and 10.6 mm in *Y*), equal to 0.31 kJ (*X*) and 0.25 kJ (*Y*), respectively. Based on these data, n_c results to be about 4.2 in *X*, and 6.7 in *Y*. Both values are included in the interval ([4,8]), confirming that a value of 5 represents an acceptable tentative assumption for n_c when $\Delta T_{el,X(Y)}$ is greater than $\Delta T_{TC\text{-}INT,ha}$, and $S_{des} = D_{des}$.

By dividing the numerically computed maximum base shear values, $V^{HT-RS}_{X(Y)}$, by the total mass *M* of the building, the associated pseudo-acceleration values, $S^{HT-RS}_{a,X(Y)}$, can be estimated. Then, the corresponding spectral damping factors, $\left(\eta^{HT-RS}_{X(Y)}\right)^{num(V)}$, are computed by means of

Table 3
CS and *RS* conditions for the *FT* scheme: maximum displacements $u_{X(Y)}^{FT-RS}$ and $\rho_{u,X(Y)}^{FT-RS}$ ratios.

CS/RS	D_{des} (mm)	SDE				BDE				MCE			
		u_X^{FT-RS}(mm)	u_Y^{FT-RS}(mm)	$\rho_{u,X}^{FT-RS}$(%)	$\rho_{u,Y}^{FT-RS}$(%)	u_X^{FT-RS}(mm)	u_Y^{FT-RS}(mm)	$\rho_{u,X}^{FT-RS}$(%)	$\rho_{u,Y}^{FT-RS}$(%)	u_X^{FT-RS}(mm)	u_Y^{FT-RS}(mm)	$\rho_{u,X}^{FT-RS}$(%)	$\rho_{u,Y}^{FT-RS}$(%)
FT-CS	16.5	11.0	11.6	0.33	0.35	27.6	24.0	0.84	0.73	35.0	31.0	1.06	0.94
FT-RS	16.5	7.6	7.1	0.23	0.21	16.9	14.9	0.51	0.45	22.7	21.2	0.69	0.64

(3a). The resulting values are equal to 0.4 in X—$(\eta_X^{HT-RS})^{num(V)}$—, and 0.35 in Y—$(\eta_Y^{HT-RS})^{num(V)}$—, both below the above-mentioned 0.55 lowest scaling factor of normative elastic response spectra.

By hypothetically referring to 0.4 and 0.35 values, the spectral displacements $S_{d,X(Y)}^{HT-RS}$ given by (2), or (4a), would be equal to 8.5 mm (X) and 7.5 mm (Y), respectively, which are notably lower than the maximum displacements deriving from the numerical analyses, equal to 18 mm in X—u_X^{HT-RS}—and 14.6 mm in Y—u_Y^{HT-RS}. Consequently, the spectral scaling factor and equivalent damping coefficient values corresponding to $u_{X(Y)}^{HT-RS}$, $\left(\eta_{X(Y)}^{HT-RS}\right)^{num(u)}$ and $\left(\xi_{X(Y)}^{HT-RS}\right)^{num(u)}$, are significantly smaller than the ones corresponding to the 0.4 and 0.35 $\eta_{X(Y)}^{HT-RS}$ values. Indeed, by extracting the scaling factors from relation (1), where S_a is deduced from (2) by putting S_d as equal to the $u_{X(Y)}^{HT-RS}$ values above, and by evaluating the equivalent damping coefficients from the damping factors, the following $\left(\eta_{X(Y)}^{HT-RS}\right)^{num(u)}$ and $\left(\xi_{X(Y)}^{HT-RS}\right)^{num(u)}$ values are obtained: 0.84 $(\eta_X^{HT-RS})^{num(u)}$ and 9.2 % $(\xi_X^{HT-RS})^{num(u)}$ in X, and 0.68 $(\eta_Y^{HT-RS})^{num(u)}$ and 16.4 % $(\xi_Y^{HT-RS})^{num(u)}$ in Y.

The differences observed between the two families of $(\eta_{X(Y)}^{HT-RS})^{num(V)}$, $(\xi_{X(Y)}^{HT-RS})^{num(V)}$ and $(\eta_{X(Y)}^{HT-RS})^{num(u)}$, $(\xi_Y^{HT-RS})^{num(u)}$ values highlight that a spectral approach for the design of dampers, when carried out separately in terms of forces or displacements, can generate significant errors, which must be corrected by applying specific iterative procedures.

Instead, the good correlation between theoretical and numerical results obtained in terms of dissipated energy shows that force and displacement reductions can be jointly controlled by applying the proposed energy-based approach, with satisfactory results also when torsional effects cannot be totally prevented.

7.2. Retrofit intervention in the FT hypothesis

Step 1.

As observed in Section 6.2, the fundamental translational periods of the *FT-CS* structure ($T_{el,X}^{FT-CS} = 0.503$ s, $T_{el,Y}^{FT-CS} = 0.474$ s) are acceptably close to T_C, equal to 0.427 s (Fig. 1f). The $S_{a,X}^{FT-CS}$ and $S_{a,Y}^{FT-CS}$ pseudo-acceleration values at the BDE drawn from the spectra in Fig. 9 are equal to 0.372 g ($S_{a,X}^{FT-CS}$) and 0.394 g ($S_{a,Y}^{FT-CS}$), respectively. The corresponding spectral displacements are: 23.1 mm ($S_{d,X}^{FT-CS}$) and 22 mm ($S_{d,Y}^{FT-CS}$). D_{des} is put as equal to 0.5 % of the height H_b of the building in this case too. Based on these data, equations (11) through (14) provide the following parameters: $\Delta S_{d,X}^{FT} = 6.6$ mm; $\Delta S_{d,Y}^{FT} = 5.5$ mm; $S_V = 287.5$ mm/s; $\Delta T_{el,X}^{FT} = 0.143$ s; $\Delta T_{el,Y}^{FT} = 0.118$ s; $T_{el,X}^{FT-RS} = 0.357$ s; and $T_{el,Y}^{FT-RS} = 0.356$ s.

As the $T_{el,X(Y)}^{FT-RS}$ periods nearly coincide with the $T_{el,X(Y)}^{HT-RS}$ values, the tubular profiles adopted in the *HT* hypothesis were selected also for the *FT* scheme. Therefore, the maximum shears, calculated by (16): $F_{el,X}^{FT-RS} = F_{el,Y}^{FT-RS} = F_{el}(T_C) = M \cdot S_a(T_C) = 1648.2$ kN, are equal to the values obtained for the *HT* case.

Step 2.

2.a. As a consequence, the equivalent damping forces and energy dissipation capacity of the devices coincide with the *HT*-related values too, i.e.$F_{D,X}^{FT} = F_{D,Y}^{FT} = 1097.9$ kN, $E_{D,X}^{FT} = E_{D,Y}^{FT} = 72.5$ kJ.

2.b. For $S_{des} = D_{des}$, the damping energy capacity of a single plate is the same as for *HT*: $E_{D,1p,X}^{FT} = E_{D,1p,Y}^{FT} = 0.325$ kJ. On the other hand, n_c was put as equal to 9 in this case, i.e. the minimum value in the interval ([9,14]) suggested in Section 4.2 for $\Delta T_{el,X(Y)}^{FT}$ values lower than $\Delta T_{TC-INT,ha} = 0.261$ s. Indeed, for the *FT* scheme the two fundamental period reductions are: $\Delta T_{el,X}^{FT} = 0.143$ s, $\Delta T_{el,Y}^{FT} = 0.118$ s. Thus, the total number of plates computed by relation (27) results to be: $N_{p,X}^{FT} = N_{p,Y}^{FT} \sim$

Table 4
CS and *RS* conditions for the *FT* scheme: maximum base shears $V^{FT-RS}_{X(Y)}$ and $\rho^{FT-RS}_{s,X(Y)}$ ratios.

		SDE				BDE				MCE			
CS/RS	$V_{R,X(Y)}$ (kN)	V^{FT-RS}_X(kN)	V^{FT-RS}_Y(kN)	$\rho^{FT-RS}_{s,X}$	$\rho^{FT-RS}_{s,Y}$	V^{FT-RS}_X(kN)	V^{FT-RS}_Y(kN)	$\rho^{FT-RS}_{s,X}$	$\rho^{FT-RS}_{s,Y}$	V^{FT-RS}_X(kN)	V^{FT-RS}_Y(kN)	$\rho^{FT-RS}_{s,X}$	$\rho^{FT-RS}_{s,Y}$
FT-CS	550.3	566	605	1.03	1.10	1373	1509	2.49	2.74	1802	1916	3.27	3.48
FT-RS	550.3	575	518	1.04	0.94	1110	1115	2.02	2.03	1469	1486	2.67	2.69

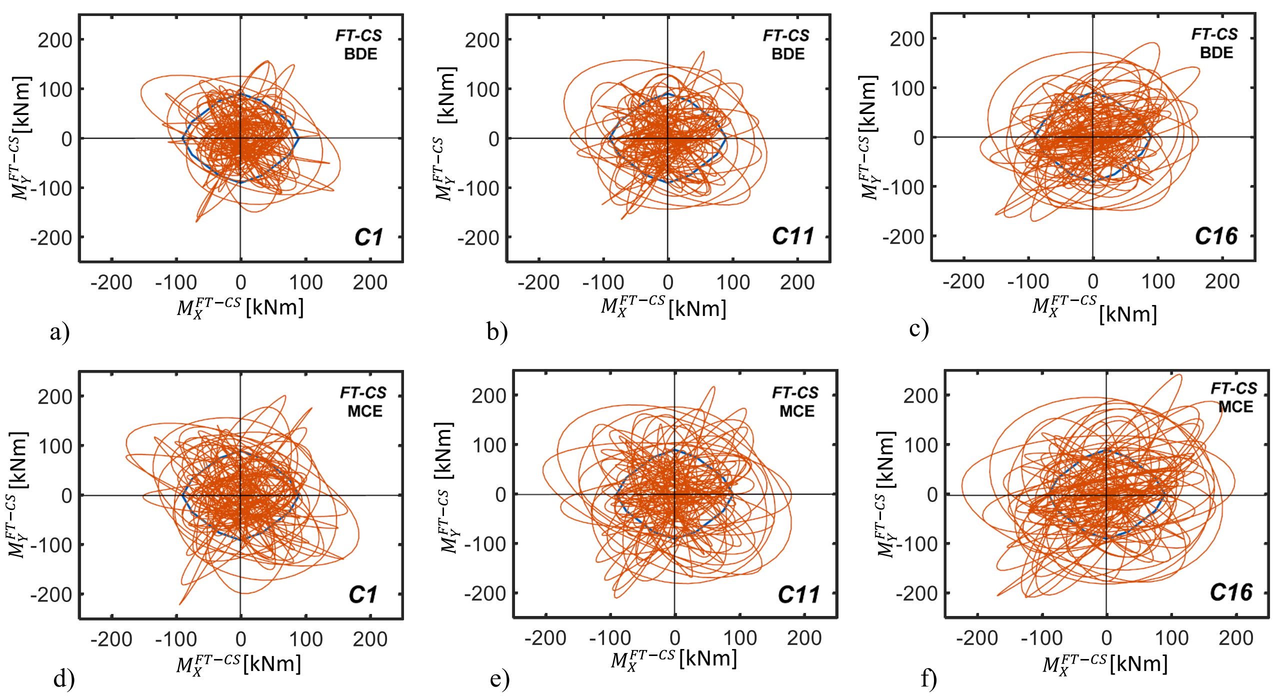

Fig. 11. *FT-CS* structure. M^{FT-CS}_X–M^{FT-CS}_Y biaxial moment interaction curves at the base section of C1, C11, and C16 columns obtained from the most demanding BDE-scaled (a, b, c) and MCE-scaled (d, e, f) groups of accelerograms, and relevant biaxial moment safe domains.

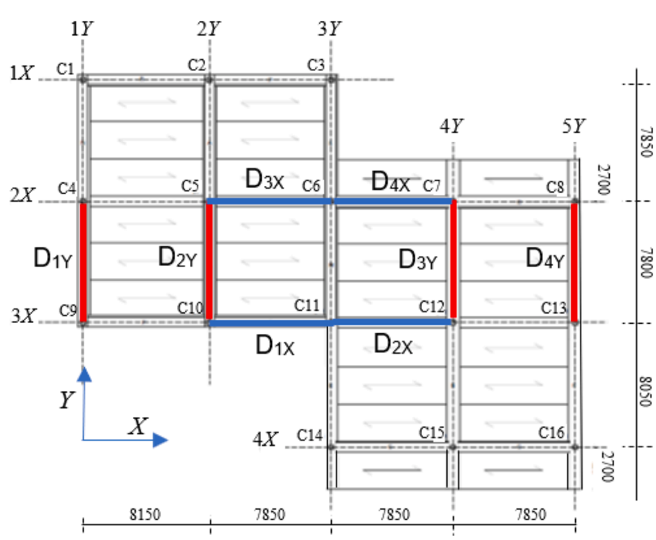

Fig. 12. Dissipative bracing system alignments in plan.

24, which is assumed as tentative design value. As it is half the value obtained for the *HT* hypothesis, the plates are assembled in groups of 6 per damper, instead of 12, and installed in the same 4 bays of the building (Fig. 12).

Step 3.

3.a. By applying relation (28) for 6 plates, the following elastic stiffness of each T-ADAS device results: $k^{FT-RS}_{i,A,X} = k^{FT-RS}_{i,A,Y} = 6{\cdot}k_{P,e} = 6{\cdot}2625.7 = 15754$ kN/m. By combining this value with the stiffness of each brace: $k^{FT-RS}_{i,el,X} = k^{FT-RS}_{i,el,Y} = 25201$ kN/m (equal to the *HT* case), the stiffness values of the dissipative system, $k^{FT-RS}_{i,DA,X}$ and $k^{FT-RS}_{i,DA,Y}$, are both equal to 9694 kN/m. Therefore, the increased stiffness produced by the 4 + 4 dissipative braces is: $K^{FT-RS}_{DA,X} = K^{FT-RS}_{DA,Y} = 38{,}776$ kN/m. As $K^{FT-CS}_{el,X}$ and $K^{FT-CS}_{el,Y}$ are equal to 61,702 kN/m and 68,598 kN/m, respectively, the following fundamental periods of the retrofitted structure result from (30): $T^{FT-RS}_{DAS,X} = 0.392$ s; $T^{FT-RS}_{DAS,Y} = 0.379$ s.

3.b. The modal analysis shows two first translational modes along *X* and *Y*, with vibration periods of 0.409 s (*X*), and 0.394 s (*Y*), and EMMs equal to 97 % (*X*), and 92 % (*Y*), respectively. The third mode is purely rotational around *Z*, with period of 0.356 s, and EMM equal to 92 %. Similarly to the *HT* hypothesis, differences no greater than 4 % (3.9 % in *X*, and 3.8 % in *Y*) are found, as compared to the values estimated by the procedure, $T^{FT-RS}_{DAS,X(Y)}$.

Table 3 duplicates, for the *FT* scheme, the results listed in Table 1 for the *HT* one. At the SDE, the maximum $\rho^{FT-RS}_{u,X(Y)}$ values are: 0.23 % in *X* and 0.21 % in *Y*, both lower than 0.33 % Operational level-associated drift limitation. The BDE and MCE-related $\rho^{FT-RS}_{u,X(Y)}$ values are: 0.51 % (*X*) and 0.45 % (*Y*)—BDE; 0.69 % (*X*) and 0.64 % (*Y*)—MCE, assessing no damage to columns for both levels, and negligible (BDE) and low (MCE) damage to infills and partitions, like in the *HT* case. The reduction factors on the drift ratios as compared to current conditions are equal to 39 % (*X*) and 38 % (*Y*) at the BDE, and 35 % (*X*) and 32 % (*Y*) at the MCE. It is worth noting that these values are smaller than for the *HT* scheme,

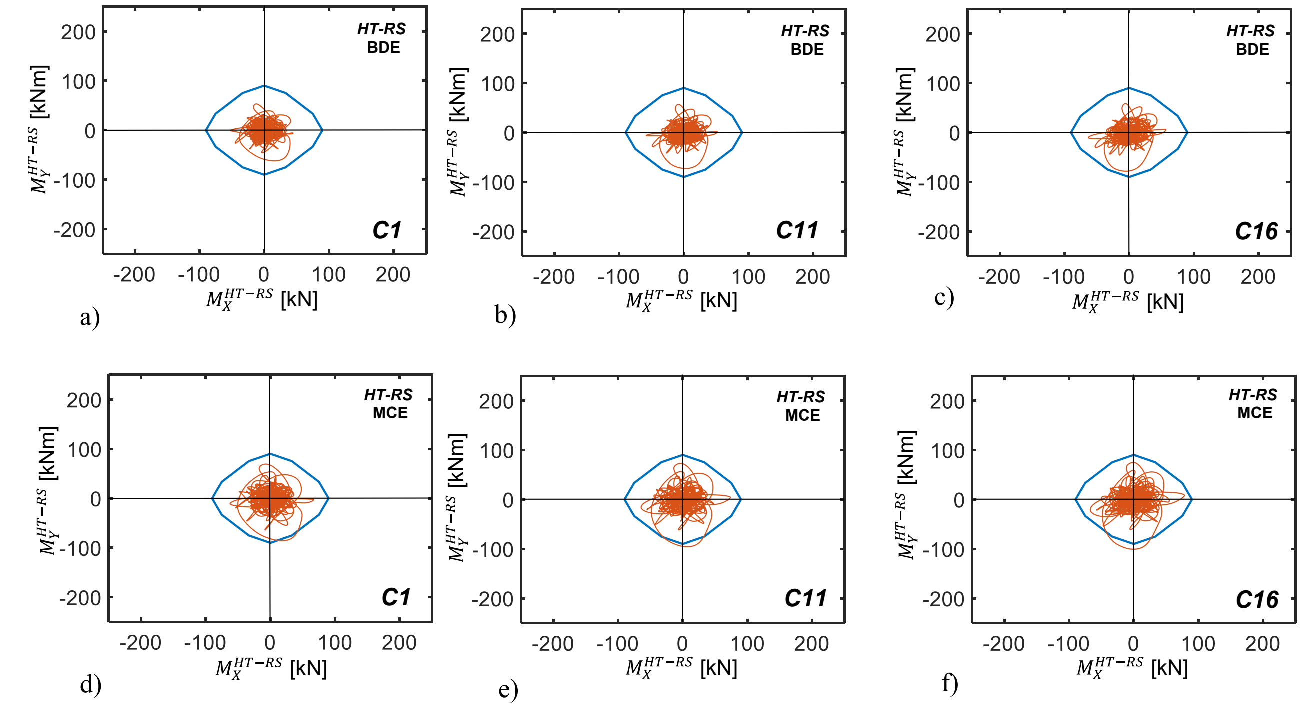

Fig. 13. *HT-RS* structure. $M_X^{HT-RS} - M_Y^{HT-RS}$ biaxial moment interaction curves at the base section of C1, C11, and C16 columns obtained from the most demanding BDE-scaled (a, b, c) and MCE-scaled (d, e, f) groups of accelerograms, and relevant biaxial moment safe domains.

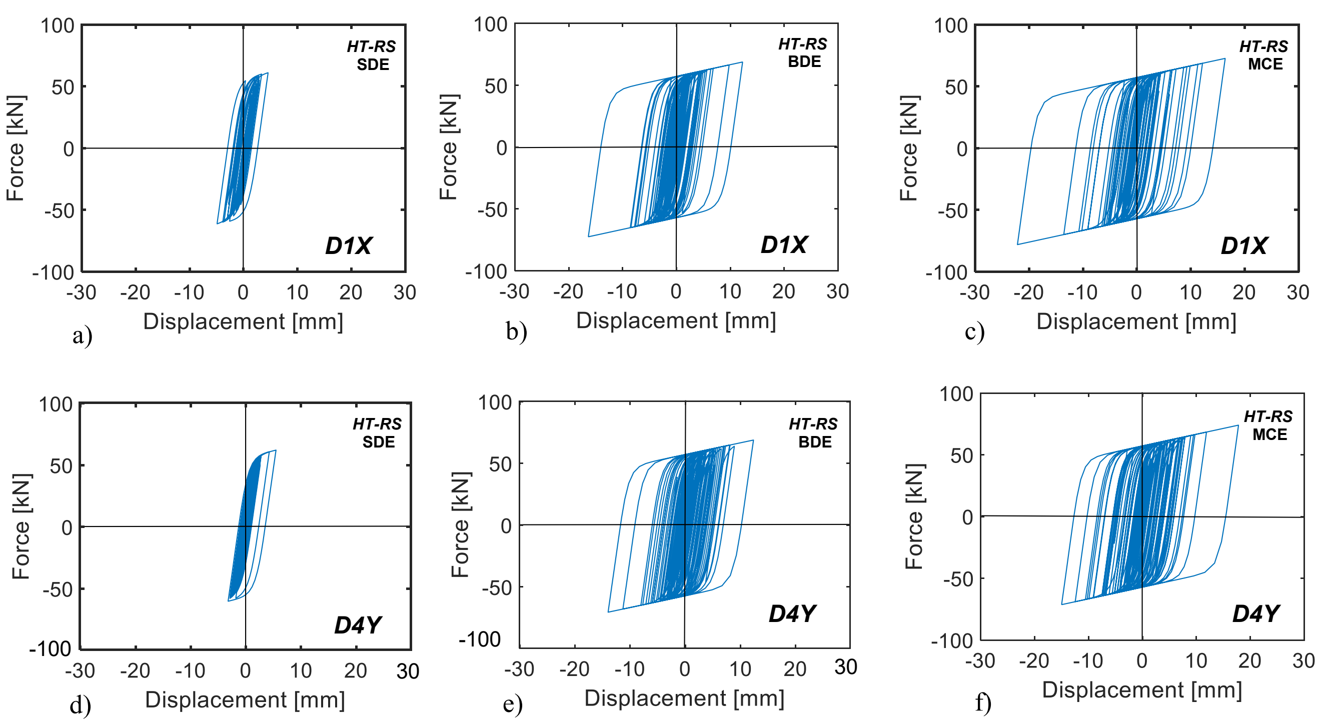

Fig. 14. *HT-RS* structure. Hysteretic cycles of D1X and D4Y dampers obtained from the most demanding SDE-scaled (a, d), BDE-scaled (b, e) and MCE-scaled (c, f) groups of accelerograms.

characterized by a considerably lower lateral stiffness.

The maximum base shears $V_{X(Y)}^{FT-RS}$, and their ratios to relevant strength values, $\rho_{V,X(Y)}^{FT-RS}$, summarized in the bottom line of Table 4, highlight values of about 2 for the latter at the BDE, with reductions no greater than 35 % as compared to current conditions. Since the corresponding reductions in terms of maximum displacements are equal to 62 %, these data confirm that the stiffening effects induced by a T-ADAS-based retrofit intervention in an originally stiff building can generate base shear reductions not fully meeting the design objectives, also when they are met in terms of displacements.

Consistently with these observations, the biaxial bending moment histories at the base of the reference columns C1, C11 and C16, graphed in Fig. 15, highlight maximum values exceeding the safe domain

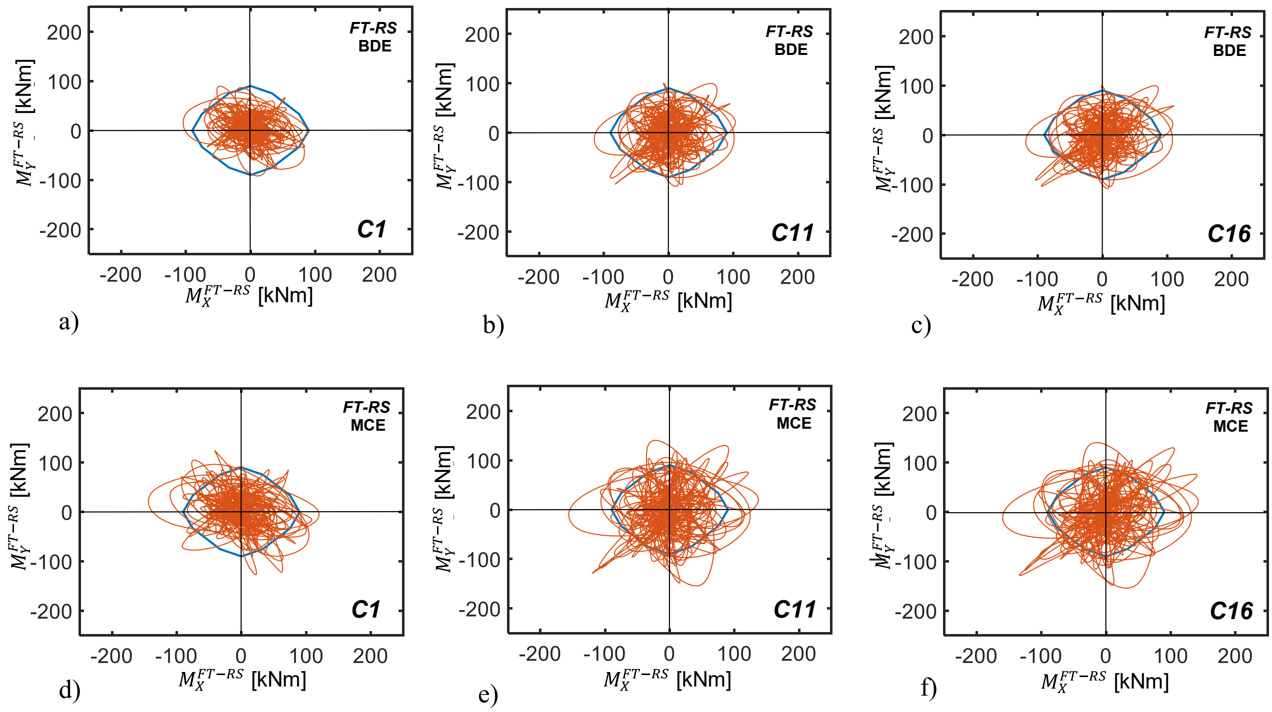

Fig. 15. *FT-RS* structure. $M_X^{FT-RS} - M_Y^{FT-RS}$ biaxial moment interaction curves at the base section of C1, C11, and C16 columns obtained from the most demanding BDE-scaled (a, b, c) and MCE-scaled (d, e, f) groups of accelerograms, and relevant biaxial moment safe domains.

boundary also for the BDE, with peaks of 32 % around X and 20 % around Y, for the most stressed column C16.

The response cycles plotted in Fig. 16 show a slightly lower plastic activity of the dampers mounted along X, which is reflected in terms of dissipated energies. By way of example, for the most severe BDE-scaled group of accelerograms, the energy associated with the response of the D_{1X}-D_{4X} devices is equal to 60 kJ, whereas the energy relevant to the D_{1Y}-D_{4Y} dampers is equal to 66.7 kJ, with a difference of about 10 %.

These values are 20.7 % (X), and 8.7 % (Y) lower than the $E_{D,X(Y)}^{FT}$ ones evaluated at the design stage. By computing the total dissipated energy for the two axes, the difference between the estimated E_D^{FT}(E_D^{FT} = 126.7 kJ), and numerical $(E_D^{FT})^{num}$ values, with $(E_D^{FT})^{num}$ = 145 kJ, is of 14.4 %.

Similar to the *HT* scheme, the total number of equivalent cycles n_c is evaluated by referring to the maximum total energy dissipated by a single plate, in the BDE-related time-history analyses, equal to 2.5 kJ in X, and 2.93 kJ in Y. By dividing these values by the energy dissipated in

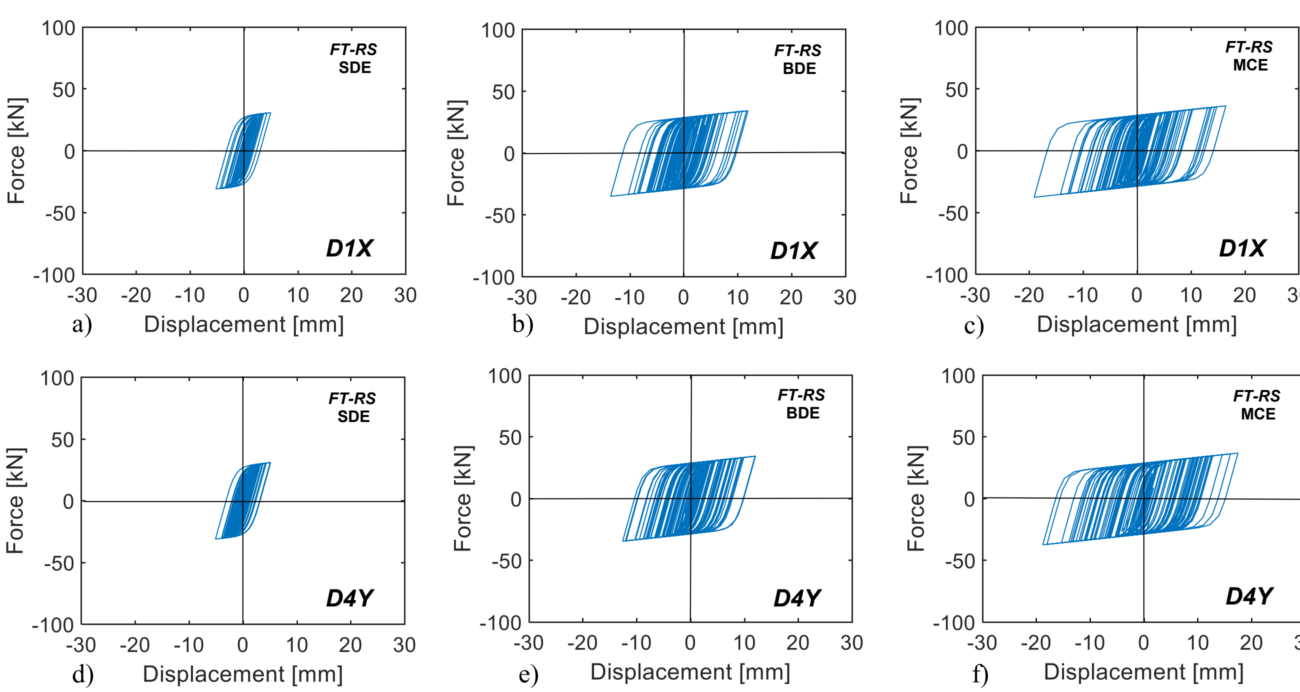

Fig. 16. *FT-RS* structure. Hysteretic cycles of D1X and D4Y dampers obtained from the most demanding SDE-scaled (a, d), BDE-scaled (b, e) and MCE-scaled (c, f) groups of accelerograms.

the cycle characterized by the maximum plastic displacement (11.3 mm in X, and 9.9 mm in Y), equal to 0.26 kJ (X) and 0.23 kJ (Y), n_c results to be equal to 9.6 in X and 12.7 in Y. As both values belong to the reference ([9,14]) interval, the $n_c = 9$ tentative assumption, for $\Delta T_{el,X(Y)} \leq \Delta T_{TC\text{-}INT,ha}$, is validated for the examined case study.

The spectral damping factors $\left(\eta_{X(Y)}^{FT-RS}\right)^{num(V)}$ derived from the numerical base shear values $V_{X(Y)}^{FT-RS}$, and related pseudo-accelerations, $S_{a,X(Y)}^{FT-RS}$, are equal to 0.66 in X—$\left(\eta_{X}^{FT-RS}\right)^{num(V)}$—and 0.67 in Y—$\left(\eta_{Y}^{FT-RS}\right)^{num(V)}$—, both greater than the 0.55 limit.

The spectral displacements $S_{d,X(Y)}^{FT-RS}$ estimated by (2) are equal to 12 mm (X) and 11.2 mm (Y), i.e. 28 % (X) and 24 % (Y) smaller than the maximum displacements computed by the numerical analysis, equal to 16.9 mm in X—u_X^{FT-RS}—and 14.9 mm in Y—u_Y^{FT-RS}. The corresponding spectral damping factors, $\left(\eta_{X(Y)}^{FT-RS}\right)^{num(u)}$, and equivalent damping coefficients, $\left(\xi_{X(Y)}^{FT-RS}\right)^{num(u)}$, are: 0.73 $\left(\eta_{X}^{FT-RS}\right)^{num(u)}$ and 13.6 % $\left(\xi_{X}^{FT-RS}\right)^{num(u)}$ in X, and 0.70 $\left(\eta_{Y}^{FT-RS}\right)^{num(u)}$ and 15.1 % $\left(\xi_{Y}^{FT-RS}\right)^{num(u)}$ in Y.

The differences between the two families of $\eta_{X(Y)}^{FT-RS}$ and $\xi_{X(Y)}^{FT-RS}$ values confirm the non-uniqueness of the definition of the equivalent damping parameters deriving from a direct spectral approach, as observed above for the *HT-RS* case.

In order to discuss further the validity of the assumption of a n_c value included in the interval [9,14] when $\Delta T_{el,X(Y)}$ is lower than $\Delta T_{TC\text{-}INT,ha}$, a different *FT-RS* solution (named *FT-RS2*) is analyzed here, which consists in adopting a total number of plates referred to $n_c = 5$, instead of 9. This determines $N_{p,X(Y)}^{FT-RS2}$ values equal to about 45 for both directions, similarly to the *HT-RS* scheme. Therefore, a final choice of 4 + 4 devices with 12 plates each is selected in this case too. Based on this tentative sizing, the results relevant to the *FT-RS2* solution are synthesized below.

- As visualized in Fig. 17, the retrofit intervention causes maximum M_X^{FT-RS2}, M_Y^{FT-RS2} moments in the most stressed column C16 still exceeding, at the BDE, the safe domain, but by no more than 3.3 % around X, and 15 % around Y, with a small improvement as compared to the *FT-RS* solution.
- The total energy dissipated by the dampers is equal to 67.4 kJ in X, and 43,8 kJ in Y, i.e. 93 % (X) and 60 % (Y) of the $E_{D,X(Y)}^{FT}$ design values. The about 40 % difference between the E_D^{FT} contributions in X and Y highlights that the damping capacity of D_{1Y}-D_{4Y} devices is underutilized, as they behave mainly like stiffening elements. This produces also an increase in torsional effects in plan. Due to the lower performance of the dampers in Y, the suitability of the design assumption for n_c is checked only for the devices installed in X. Based on the results of the time-history analyses, a value of 9.4 is found, which confirms further the assumption of a value included in the interval ([9,14]) when $\Delta T_{el,X(Y)}$ is lower than $\Delta T_{TC\text{-}INT,ha}$.
- By comparing the numerical results obtained for the *FT-RS* and *FT-RS2* schemes, the greater number of plates adopted for the latter reduces the energy dissipated by each plate and increases the stiffness of the retrofitted building. In particular, when the stiffness determines fundamental translational periods equal to or lower than T_C, steel dampers work mainly as stiffening devices, as observed above. This is confirmed by the graphs in Fig. 18, where the time histories of the input (E_I) and dissipated (E_D) energies obtained for the *FT-RS* and *FT-RS2* solutions are plotted in superposition for the most severe SDE-, BDE-, MCE-scaled accelerograms. Indeed, these graphs show that the double number of plates selected for the *TF-RS2* design hypothesis increases the input energy by 18.2 % (SDE), 9.5 % (BDE), and 11.9 % (MCE), and reduces the dissipated energy by 50.7 % (SDE), 8.6 % (BDE), and 10.6 % (MCE).

8. Conclusions

The design procedure of steel dampers incorporated in dissipative bracing systems for the seismic retrofit of frame structures formulated in this study, and demonstratively detailed for T-ADAS devices, is conceived for any type of steel hysteretic dampers characterized by joint stiffening and damping elasto-plastic properties. In order to properly exploit both properties, the procedure initially targets to constrain lateral displacements below an assumed design limit, S_{des}, by increasing

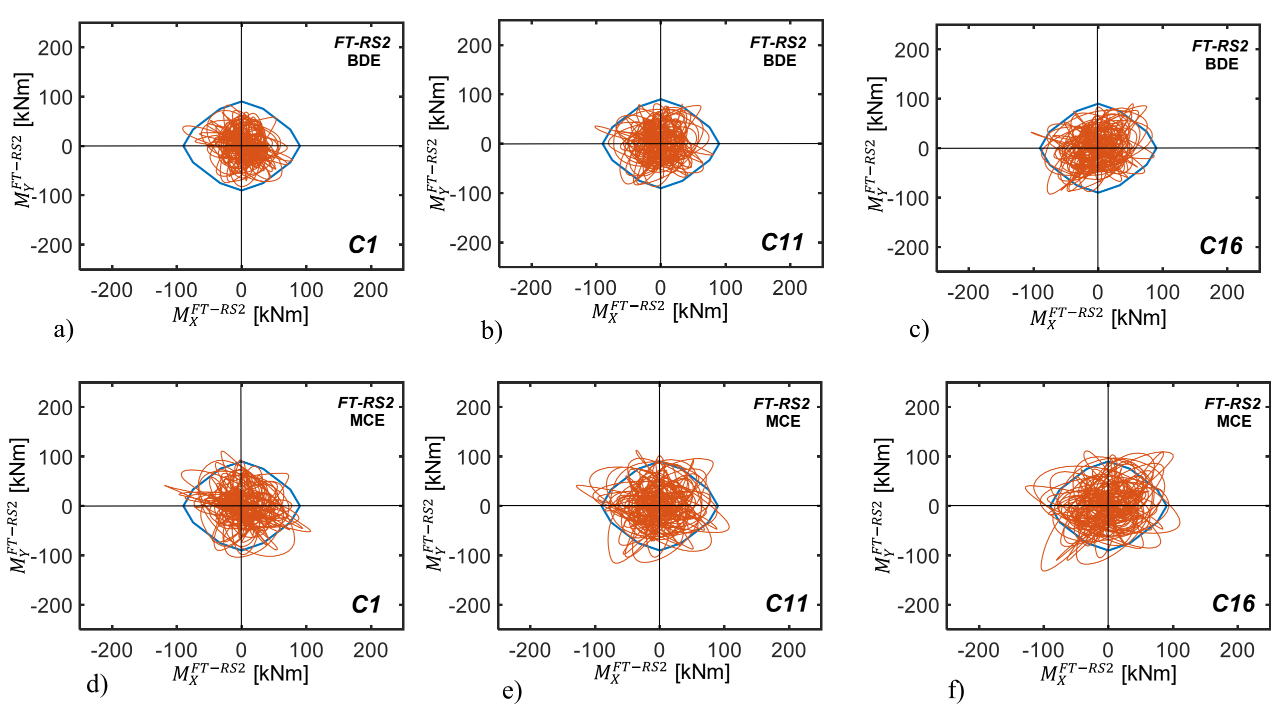

Fig. 17. *FT-RS2* structure. M_X^{FT-RS2} – M_Y^{FT-RS2} biaxial moment interaction curves at the base section of C1, C11, and C16 columns obtained from the most demanding BDE-scaled (a, b, c) and MCE-scaled (d, e, f) groups of accelerograms, and relevant biaxial moment safe domains.

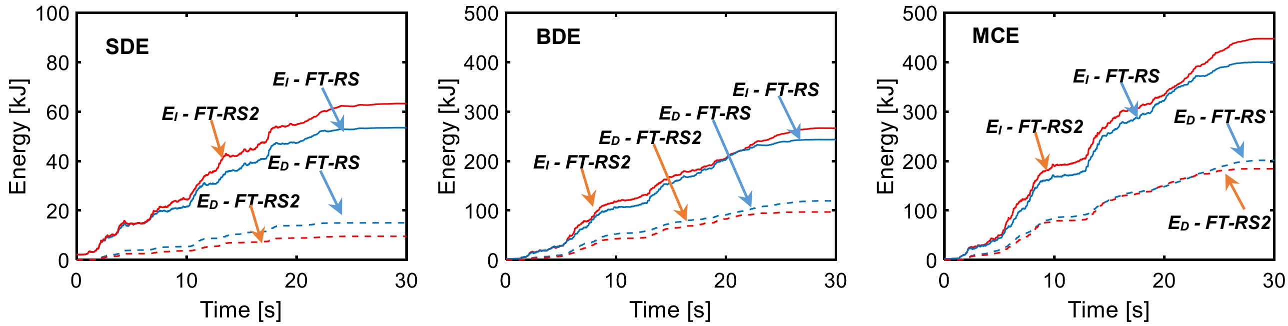

Fig. 18. Input and dissipated energies for the *FT-RS* and *FT-RS2* retrofit solutions, obtained for the most demanding SDE-scaled, BDE-scaled and MCE-scaled groups of accelerograms.

the translational stiffness of the original structure. Afterwards, the procedure tentatively estimates the damping capacity of the dissipaters needed to reduce base shears below the corresponding strength values computed for the two reference axes in plan. As shown, the evaluation of the $E_{D,X(Y)}$ energy dissipation capacity of the devices depends on the correlation between the $\Delta T_{el,X(Y)}$ fundamental period reductions caused by the retrofit intervention and the $\Delta T_{TC-INT,ha}$ reference period reduction. The latter is equal to half the difference between the T_{INT} period corresponding to the intersection of the pseudo-acceleration and displacement spectra and the T_C initial period of the constant pseudo-velocity spectrum branch.

In the case of T-ADAS devices, this correlation directly influences the estimation of the number of plates needed to attain the targeted $E_{D,X(Y)}$ values, which are a function of the number of equivalent cycles n_c. Indeed, it is demonstrated in the study that n_c varies from 4 to 8 when $\Delta T_{el,X(Y)}$ is greater than $\Delta T_{TC-INT,ha}$, and from 9 to 14 when $\Delta T_{el,X(Y)}$ is smaller than $\Delta T_{TC-INT,ha}$. This result provides more specific choice criteria for n_c within the ([4,14]) range already suggested in the literature.

The single-storey school building analyzed as demonstrative case study allowed to explicate the application of the procedure in practice, as well as to integrate the general considerations underlying its formulation, as recapitulated below.

- By comparing the performance obtained for the two hypotheses of hinged or fixed-end roof beam-to-column connections of the precast RC structure, it is shown that the effectiveness of the hysteretic devices decreases as the fundamental vibration periods in retrofitted conditions decrease, and particularly when the periods become smaller than T_C.
- For the *HT* scheme, when $\Delta T_{el,X(Y)}$ is greater than $\Delta T_{TC-INT,ha}$, the design assumption $n_c = 5$ results to be satisfactory. A greater exploitation of the hysteretic capacity of dampers, reached for greater plastic response displacements, tends to locate n_c in proximity to the lower boundary of the ([4,8]) interval, as checked in *X* direction, where the computed n_c value is equal to 4.2. For smaller displacements, like the ones obtained in *Y*, n_c tends to approach the upper boundary of the interval (as assessed by a value of 6.7 for this axis).
- The target performance in terms of lateral displacements, base shears, and maximum moments at the base of columns was met for the *HT* scheme with only a minimum difference (1.3 %) between the tentatively estimated and the computed values of the total energy dissipated by the dampers. On the other hand, the analysis of this less stiff structural configuration—which causes a higher energy dissipation demand on the T-ADAS devices—shows that the estimation of the equivalent linear viscous damping ξ for the protective system can provide notably different results depending on whether it is carried out in terms of forces (i.e. accelerations) or displacements. This confirms the need for iterative sizing approaches when the design is developed separately for the two quantities, while such need is bypassed by their joint control included in the proposed energy-based procedure.
- For the *FT* scheme, where—unlike in the *HT* one—$\Delta T_{el,X(Y)}$ is smaller than $\Delta T_{TC-INT,ha}$, the assumption of a n_c value equal to 9 effectively predicts the energy dissipation demand on the dampers when the latter matches the energy value estimated at the sizing stage, as it occurs for the *X* direction. Instead, when the energy dissipation computed by the time-history analyses is notably smaller than the target design value, as observed in the *Y* direction, n_c approaches the upper boundary of the ([9,14]) range (reaching a value of 12.7 in the considered case).
- The analyses carried out for the *FT* scheme also highlight that, when the lateral displacements of the structure in current conditions are small, i.e. below 0.5 % of its height, as surveyed for the *FT-RS* scheme, the $T^{RS}_{el,X(Y)}$ period in retrofitted conditions can be smaller than T_C. When this occurs, it may be preferable to install conventional elastic braces, instead of dissipative ones, since T-ADAS devices work essentially as stiffening elements, rather than damping devices.

CRediT authorship contribution statement

Gloria Terenzi: Conceptualization, Methodology, Validation, Writing – review & editing, Supervision, Funding acquisition, Software, Investigation, Data curation, Visualization.

Declaration of Competing Interest

The author declares that she has no known competing financial interests or personal relationships that could have appeared to influence the work reported in this paper.

Data availability

Data will be made available on request.

Acknowledgements

The study reported in this paper was financed by the Italian Department of Civil Protection within the ReLUIS-DPC Project 2022/2024 – Research Line 15: Normative Contributions for Isolation and Dissipation. The authors gratefully acknowledge this financial support.

References

[1] Hanson RD, Soong TT. Seismic design with supplemental energy dissipation devices. Publication MNO-8 EERI–Earthquake Engineering Research Center: Oakland, CA, 2001.

[2] Soong TT, Spencer BF. Supplemental energy dissipation: state-of-the-art and state-of-the-practice. Eng Struct 2002;24(3):243–59.
[3] Christopoulos C, Filiatrault A. Principles of passive supplemental damping and seismic isolation. IUSS PRESS, Pavia, Italy, 2006; ISBN: 88-7358-037-8.
[4] Lazan BJ. Damping of materials and members in structural mechanics, Pergamon Eds, Oxford, 1968.
[5] Sorace S, Terenzi G. Seismic protection of frame structures by fluid viscous damped braces. ASCE J Struct Eng 2008;134(1):45–55.
[6] Aiken ID, Nims DK, Whittaker AS, Kelly JM. Testing of passive energy dissipation systems. Earthq Spectra 1993;9(3):335–70.
[7] Ramirez OM, Costantinou MC, Whittaker AS, Kircher CA, Chrysostomou CZ. Elastic and inelastic seismic response of buildings with damping systems. Earthq Spectra 2002;18(3):531–47.
[8] Mazza F, Mazza M, Vulcano A. Displacement-based seismic design of hysteretic damped braces for retrofitting in-elevation irregular r.c. framed structures. Soil Dyn and Earthq Eng 2015;69(115124).
[9] Hyderuddin M, Imran MM, Mohsin S. Retrofitting of reinforced concrete frames using steel bracing. Int J Sc Res Dev 2016;4(08):297.
[10] Terenzi G. Energy-based design criterion of dissipative bracing systems for seismic retrofit of framed structures. Appl Sci 2018;8(2):268.
[11] Terenzi G, Bazzani C, Costoli I, Sorace S, Spinelli P. Advanced seismic retrofit of a mixed R/C-Steel structure. Buildings 2019;9(12):241.
[12] Sorace S, Terenzi G. Roof isolation and girder-to-column dissipative connections in seismic design of precast R/C structures. Infrastructures 2020;5(11):104.
[13] Terenzi G, Costoli I, Sorace S. Activation control extension of a design method of fluid viscous dissipative bracing systems. Bull Earthq Eng 2020;18(8):4017–38.
[14] Constantinou MC, Symans MD. Experimental study of seismic response of buildings with supplemental fluid dampers. J Struct Des Tall Buildings 1993;2(2):93–132.
[15] Ramirez OM, Constantinou MC, Whittaker AS, Kircher CA, Johnson MW, Chrysostomou CZ. Validation of the 2000 NEHRP provisions' equivalent lateral force and modal analysis procedures for buildings with damping systems. Earthq Spectra 2003;19(4):981–99.
[16] Whittaker A, Costantinou M, Ramirez O, Johnson M, Chrysostomou C. Equivalent lateral force and modal analysis procedures for the 2000 NEHRP provisions for buildings with damping systems. Earthq Spectra 2003;19(4):959–80.
[17] ASCE/SEI 41-17. Seismic evaluation and retrofit of existing buildings. American Society of Civil Engineers – Structural Engineering Institute: Reston, VA, 2017.
[18] Silvestri S, Gasparini G, Trombetti T. A five-step procedure for the dimensioning of viscous dampers to be inserted in building structures. J Earthq Eng 2010;14: 417–47.
[19] Palermo M, Silvestri S, Landi L, Gasparini G, Trombetti T. A "direct five-step procedure" for the preliminary seismic design of buildings with added viscous dampers. Eng Struct 2018;173:933–50.
[20] Nuzzo I, Losanno D, Caterino N. Seismic design and retrofit of frame structures with hysteretic dampers: a simplified displacement-based procedure. Bull Earthq Eng 2019;17(5):2787–819.
[21] Di Sarno L, Wu J-R. Evaluation of seismic performance of existing steel moment-resisting frames: a case study, Proc of SECED 2019 Conference, London, 9-10 September, 2019.
[22] Mazza F. Combination of different types of damped braces for two-level seismic control of r.c. framed buildings. J Build Eng 2021;44(103268).
[23] Mazza F. Nonlinear seismic analysis of unsymmetric-plan structures retrofitted by hysteretic damped braces. Bull Earthq Eng 2016;14(4):1311–31.
[24] Mazza F. In-plan and out-of-plane nonlinear seismic response of masonry infills for hospitals retrofitted with hysteretic damped braces. Soil Dyn and Earthq Eng 2021; 148:106803.
[25] Sorace S, Terenzi G, Fadi F. Shaking table and numerical seismic performance evaluation of a fluid viscous-dissipative bracing system. Earthq Spectra 2012;28 (4):1619–42.
[26] Sorace S, Terenzi G, Licari M. Traditional and viscous dissipative steel braced top addition strategies for a R/C building. Int J Struct Eng 2015;6(4):332–53.
[27] Sorace S, Terenzi G, Mori C. Passive energy dissipation-based retrofit strategies for R/C frame water towers. Eng Struct 2016;106:385–98.
[28] Karavasilis LT, Kerawala S, Hale E. Hysteretic model for steel energy dissipation devices and evaluation of a minimal-damage seismic design approach for steel buildings. J Cost Steel Res 2012;70:358–67.
[29] Teruna DR, Majid TA, Budiono B. Experimental Study of Hysteretic Steel Damper for Energy Dissipation Capacity. Adv Civ Eng 2015;ID 631726:12 pages.
[30] Khoshkalam M, Mortezagholi MH, Zahrai SM. Proposed modification for ADAS damper to eliminate axial force and improve seismic performance. J Earthq Eng 2022;26(10):5130–52.
[31] TahamaouliRoudsari M, Eslamimanesh MB, Entezari AR, Noori O, Torkaman M. Experimental assessment of retrofitting RC moment resisting frames with ADAS and TADAS yelding dampers. Structures 2018;14:75–87.
[32] Technical Standards on Constructions [in Italian]. Italian Council of Public Works, Rome, Italy, 2018.
[33] Jacobsen LS Damping in composite structures. Proc of the 2nd WCEE, Tokyo and Kyoto, 1960; vol. II: 1029-1044.
[34] Newmark NM, Hall WJ. Earthquake Spectra and Design. EERI, Oakland, CA: Engineering Monographs; 1982.
[35] Chopra AK. Elastic response spectrum; A historical note. Earthq Eng Struct Dyn 2007;36:3–12.
[36] Priestley MJN, Calvi GM, Kowalsky MJ. Displacement Based Seismic Design of Structures. Pavia: IUSS Press; 2007.
[37] Martinez-Romero E. Experiences on the use of supplemental energy dissipators on building structures. Earthq Spectra 1993;9(3):581–624.
[38] Dargush GF, Soong TT. Behavior of metallic plate dampers in seismic passive energy dissipation systems. Earthq Spectra 1995;11(4):545–68.
[39] Ribakov Y, Gluck J. Optimal design of ADAS damped MDOF structures. Earthq Spectra 1999;15(2):317–30.
[40] Gandelli E, De Domenico D, Quaglini V. Cyclic engagement of hysteretic steel dampers in braced buildings: a parametric investigation. Bull Earthq Eng 2021;19: 5219–51.
[41] SAP2000NL. Theoretical and users' manual. Release 20.01. Computers & Structures Inc.: Berkeley, USA, 2021.
[42] Vanmarcke EH, Fenton GA, Heredia-Zavoni E. SIMQKE-II – Conditioned earthquake ground motion simulator: User's manual, version 2.1. Princeton, USA: Princeton University:; 1999.
[43] EN 1998-4. Eurocode 8: Design of structures for earthquake resistance - Part 1: general seismic rules. Seismic Actions and Rules for Buildings. European Committee for Standardisation: Brussels, Belgium, 2003.